

# Toward a general calibration of the Swiss plate geophone system for fractional bedload transport

Tobias Nicollier<sup>1,2</sup>, Gilles Antoniazza<sup>3,1</sup>, Lorenz Ammann<sup>1</sup>, Dieter Rickenmann<sup>1</sup>, James W. Kirchner<sup>1,2,4</sup>

<sup>1</sup>Swiss Federal Research Institute WSL, Birmensdorf, 8903, Switzerland

<sup>2</sup>Department of Environmental System Sciences, ETH Zürich, Zürich, 8092, Switzerland

<sup>3</sup>Institute of Earth Surface Dynamics (IDYST), University of Lausanne, Lausanne, 1015, Switzerland

<sup>4</sup>Department of Earth and Planetary Science, University of California, Berkeley, 94720, USA

*Correspondence to:* Tobias Nicollier, Swiss Federal Research Institute (WSL), Mountain Hydrology and Mass Movements, 8903 Birmensdorf, Switzerland. E-mail: tobias.nicollier@wsl.ch. Phone: +41 77 437 35 77

**Abstract.** Substantial uncertainties in bedload transport predictions in steep streams have encouraged intensive efforts to develop surrogate monitoring technologies. One such system, the Swiss plate geophone (SPG), has been deployed and calibrated in numerous steep water courses, mainly in the Alps. Calibration relationships linking the signal recorded by the SPG system to the transported bedload can vary substantially between different monitoring stations, likely due to site-specific factors such as flow velocity and bed roughness. Furthermore, recent controlled experiments on the SPG system have shown that site-specific calibration relationships can be biased by elastic waves resulting from impacts occurring outside the plate boundaries. Motivated by these findings, we present here a hybrid calibration procedure derived from flume experiments and an extensive dataset of 308 calibration measurements from four different SPG field monitoring stations. Our main goal is to investigate the feasibility of a general, site-independent calibration procedure for inferring fractional bedload transport from the SPG signal. First, we use flume experiments to show that sediment size classes can be distinguished more accurately using a combination of vibrational frequency and amplitude information than by using amplitude information alone. Second, we apply this amplitude-frequency method to field measurements to derive general calibration coefficients for ten different grain-size fractions. The amplitude-frequency method results in more homogeneous signal responses across all sites and significantly improves the accuracy of fractional sediment flux and grain-size estimates. We attribute the remaining site-to-site discrepancies to large differences in flow velocity, and discuss further factors that may influence the accuracy of these bedload estimates.

## 1 Introduction

Flood events across Europe in the summer of 2021 have illustrated the threat of flood-related hazards like bedload transport to human life and infrastructure, especially in small and steep mountainous catchments (Badoux et al., 2014; Blöschl et al., 2020). Understanding sediment transport processes is also essential for efforts to return rivers to their near-natural state by restoring their continuity and re-establishing balanced sediment budgets (e.g. Brouwer and Sheremet, 2017; Pauli et al., 2018; Logar et al., 2019; Rachely et al., 2021). However, monitoring and predicting bedload transport still represents a considerable challenge because of its large spatio-temporal variability (e.g. Mühlhofer, 1933; Einstein, 1937; Reid et al., 1985; Rickenmann, 2018; Ancy, 2020). This is especially true for steep streams, because they are poorly described by traditional bedload transport equations, which have mainly been developed for lower-gradient channels (e.g. Schneider et al.,

39 2016). Predicting sediment transport in steep channels is challenging, notably due to the presence of macro-roughness  
40 elements affecting both the flow resistance and the flow energy (e.g. Manga and Kirchner, 2000; Yager et al., 2007, 2012;  
41 Bathurst, 2007; Nitsche et al., 2011; Rickenmann and Recking, 2011; Prancevic and Lamb, 2015). It is further complicated  
42 by a sediment supply that varies in both space and time, due in part to cycles of building and breaking of an armoring layer  
43 at the riverbed (e.g. Church et al., 1998; Dhont and Ancey, 2018; Rickenmann, 2020; Piantini et al., 2021).

44 Bedload transport equations established for lower-gradient streams typically result in multiple order-of-magnitude  
45 errors when applied to steep streams, motivating the development of new indirect monitoring techniques for steep mountain  
46 channels (e.g. Gray et al., 2010; Rickenmann, 2017). Indirect monitoring techniques provide large spatial coverage of river  
47 transects at high temporal resolution, reduce personal risk related to in-stream sampling, and enable consistent data  
48 collection at widely varying flow conditions, including during flooding events (e.g. Gray et al., 2010; Rickenmann, 2017;  
49 Geay et al., 2020; Bakker et al., 2020; Choi et al., 2020; Le Guern et al., 2021). The drawback of these monitoring  
50 technologies is that in order to provide quantitative measurements, they often require intensive calibration through direct  
51 bedload sampling with retention basins (Rickenmann and McArdeell, 2008), slot samplers (e.g. Habersack et al., 2017; Halfi  
52 et al., 2020) or mobile bag samplers (e.g. Bunte et al., 2004; Dell'Agnese et al., 2014; Hilldale et al., 2015; Mao et al., 2016;  
53 Kreisler et al., 2017; Nicollier et al., 2021).

54 Among indirect monitoring techniques, the Swiss plate geophone (SPG) system has been deployed and tested in more  
55 than 20 steep gravel-bed streams and rivers, mostly in the European Alps (Rickenmann, 2017). Typically, linear or power-  
56 law calibration relationships have been developed between measured signal properties and bedload transport characteristics  
57 (Rickenmann et al., 2014; Wyss et al. 2016a; Kreisler et al., 2017; Kuhnle et al., 2017). Such calibration equations permit  
58 absolute quantification of bedload fluxes, their variability in time and space (i.e. across a river section), estimates of bedload  
59 grain-size distribution, and the detection of the start and end of bedload transport. However, these equations require a  
60 calibration procedure against independent bedload transport measurements at each individual field site, because until now we  
61 have lacked generally applicable signal-to-bedload calibration equations that are valid across field settings. Although  
62 similarities between calibration relationships at various field sites are encouraging, it is not well understood why the linear  
63 calibration coefficients for total mass flux can vary by about a factor of 20 among individual samples from different sites, or  
64 by about a factor of six among the mean values from different sites (Rickenmann et al., 2014; Rickenmann and Fritschi,  
65 2017). Given the substantial field effort required for calibration campaigns, a generally applicable calibration equation would  
66 represent a significant advance.

67 Numerous studies have reported successful calibration of impact plate systems in laboratory flumes (e.g. Bogen and  
68 Møen, 2003; Krein et al., 2008; Tsakiris et al., 2014; Mao et al., 2016; Wyss et al., 2016b,c; Kuhnle et al., 2017; Chen et al.,  
69 2022), although transferring these flume-based calibrations to the field remains challenging. Nonetheless, controlled flume  
70 experiments are valuable because they allow to systematically explore relationships between the recorded signal, the  
71 transport rates of different sediment size fractions, and the hydraulic conditions. For example, the experiments of Wyss et al.  
72 (2016b) showed that higher flow velocities induce a weaker SPG signal response per unit of transported sediment. More  
73 recent controlled experiments have highlighted another important site-dependent factor influencing the SPG signal response,  
74 namely the grain-size distribution (GSD) of the transported bedload (Nicollier et al., 2021), where coarser grain mixtures  
75 were shown to yield a stronger signal response per unit bedload weight.

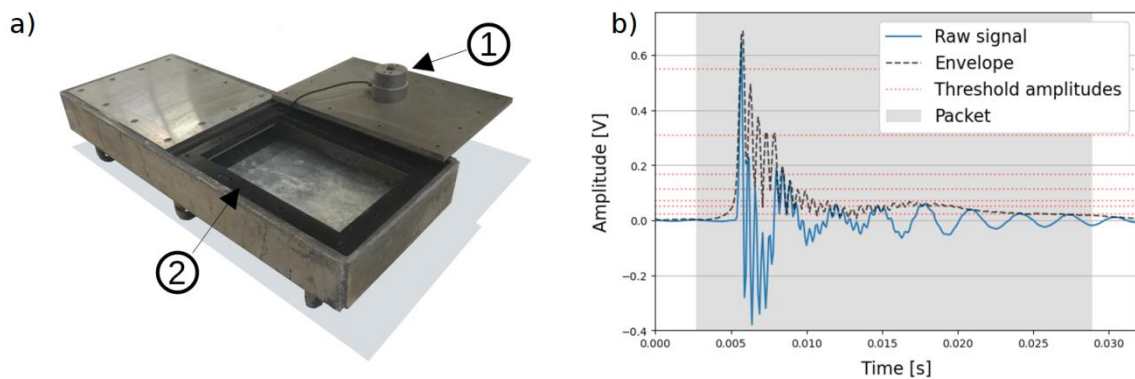
76 Subsequent impact tests and flume experiments showed that this grain-size dependence arises because the impacts  
77 plates are insufficiently isolated from their surroundings (Antoniazza et al., 2020; Nicollier et al., 2022). The elastic wave  
78 generated by an impact on or near a plate was found to propagate over several plate lengths, contaminating the signals  
79 recorded by neighboring sensors within a multiple plate array. Nicollier et al. (2022) introduced the notion of “apparent  
80 packets” (in opposition to “real” packets) to define the portions of the recorded signal that were generated by such  
81 extraneous particle impacts.

82 The main goal of this contribution is to examine the feasibility of a general, site-independent signal conversion  
83 procedure for fractional bedload flux estimates. We follow a comprehensive hybrid signal conversion approach that  
84 encompasses a set of full-scale controlled flume experiments conducted at an outdoor flume facility, as well as 308 field  
85 calibration measurements performed with direct sampling methods at four different bedload monitoring stations in  
86 Switzerland between 2009 and 2020. We present the amplitude-frequency (AF) method, aiming to reduce the bias introduced  
87 by apparent packets in the relationship between the signal characteristics and the particle size. Finally, we compare the  
88 performance of this novel AF method against the amplitude-histogram (AH) method developed by Wyss et al. (2016a) for  
89 both fractional and total bedload flux estimates.

## 90 2 Methods

### 91 2.1 The SPG system

92 The Swiss plate geophone (SPG) consists of a geophone sensor fixed under a steel plate of standard dimensions 492 mm x  
93 358 mm x 15 mm (Fig. 1a; Rickenmann, 2017). The geophone (GS-20DX by Geospace technologies; www.geospace.com)  
94 uses a magnet moving inside an inertial coil (floating on springs) as an inductive element. The voltage induced by the  
95 moving magnet is directly proportional to its vertical velocity resulting from particle impacts on the plate. The SPG system  
96 can detect bedload particles with a diameter down to 10 mm (Rickenmann et al., 2014, 2020; Wyss et al., 2016a). Typically,  
97 a SPG array includes several plates next to each other, acoustically isolated by elastomer elements and covering the river  
98 cross-section. The array is either embedded in a concrete sill or fixed at the downstream face of a check dam. A detailed  
99 description of the SPG system can be found in Rickenmann et al. (2014). For all the calibration measurements and the  
100 outdoor flume experiments analyzed in this study, ranging from a few seconds to one hour, the full raw signal 10 kHz  
101 geophone signal was recorded (Fig. 1b). In the normal operational recording mode with continuous data storage, due to data  
102 storage limitations, field stations usually do not continuously record the full raw signal, but only preprocessed summary  
103 values (Rickenmann et al., 2014).

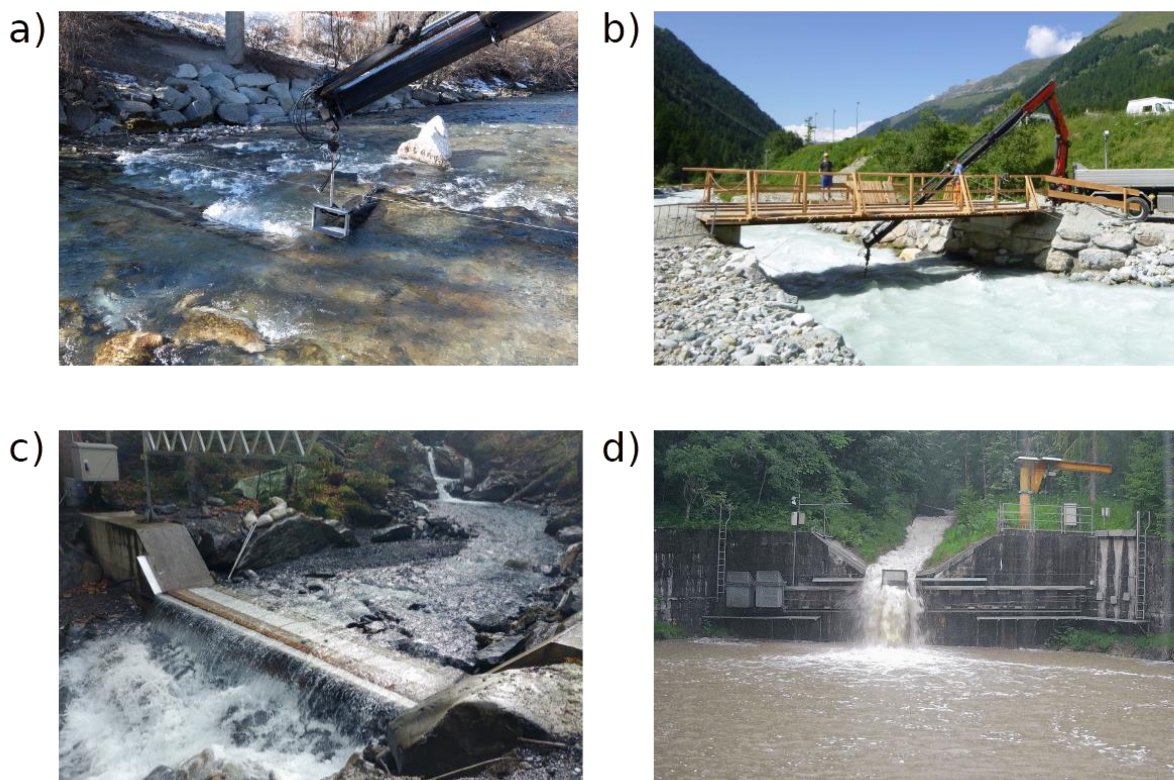


104  
105 **Figure 1:** (a) Swiss plate geophone (SPG) system before installation (see Fig. 3). Each plate is equipped with a uniaxial geophone  
106 sensor fixed in a watertight aluminum box (1) attached to the underside of the plate. The plates are acoustically isolated from each  
107 other by elastomer elements (2). (b) Example of a packet (grey area) detected by the SPG system. A packet begins 20 time steps  
108 (i.e., 2 ms) before the signal envelope crosses the lowest amplitude threshold of 0.0216 V and ends 20 time steps after the last  
109 crossing of the lowest amplitude threshold (see Sect. 2.4).

110

111 **2.2 Field calibration measurements**

112 To test the AF and AH methods, this study uses 308 calibration measurements from four Swiss bedload monitoring stations  
113 equipped with the SPG system (Fig. 2; Table 1). Field calibration samples were collected at the Albula, Navisence and  
114 Avançon de Nant stations, and extensive calibration efforts have been undertaken at the fourth field station, the Erlenbach,  
115 since 2009 (Rickenmann et al., 2012). The Erlenbach offers an interesting comparison with the other sites due to different  
116 channel and flow characteristics upstream of the SPG plates. These are the only field sites equipped with an SPG system at  
117 which the full raw geophone signal has been recorded during calibration measurements. Field calibrations carried out at the  
118 four sites consisted of the following steps: (i) direct bedload sampling downstream of an impact plate using either crane-  
119 mounted net samplers adapted from Bunte traps (Bunte et al., 2004; Dell’Agnese et al., 2014; Nicollier et al., 2019; Fig. 2a,  
120 b), automated basket samplers (Rickenmann et al., 2012; Fig. 2d) or manual basket samplers (Fig. 2c; Antoniazza et al.,  
121 2022), (ii) synchronous recording of the raw geophone signal, (iii) sieving and weighing of bedload samples using ten sieve  
122 classes (see Sect. 2.4), and (iv) comparing the fractional bedload mass of each sample to the geophone signal to derive the  
123 corresponding calibration coefficients. A more detailed description of the sampling procedure is reported in Supporting  
124 Information S1, including the mesh sizes used for bedload sampling. For the analysis, only particles larger than 9.5 mm were  
125 considered, being close to the SPG detection threshold. Streamflow information was derived from various stage sensors  
126 (Table 1). Flow velocity  $V_w$  was introduced by Wyss et al. (2016c) as a possible governing parameter affecting the number  
127 of particles detected by the SPG system. Unfortunately, due to the lack of continuous flow velocity measurements at the  
128 Albula and Navisence sites, we were not able to account for the effect of the flow velocity in the signal conversion procedure  
129 described in the present study.



130

131 **Figure 2: The four Swiss bedload monitoring stations at which raw Swiss plate geophone signals have been recorded during**  
132 **calibration measurements. The stations are installed at the following streams: a) Albula, b) Navisence, c) Avançon de Nant and d)**  
133 **Erlenbach. Pictures a) and c) were taken during low-flow conditions. Pictures b) and d) show calibration measurements with the**  
134 **crane-mounted net sampler and the automated basket sampler, respectively, at high flows.**

135

136

137

138 **Table 1: Channel and flow characteristics based on *in situ* measurements during the calibration campaigns at the four field sites.**  
 139 **The year of the field calibration campaigns, the sampling technique and the number of collected samples are also indicated.**

Field site	Location (canton)	Bed slope [%] <sup>a</sup>	Mean flow velocity $V_f$ [ $\text{m s}^{-1}$ ] <sup>b</sup>	No. of plates	Year	Sampling technique	No. of samples
Albula <sup>c</sup>	Tiefencastel (Grisons)	0.7	2.6	30	2018	crane-mounted net sampler	51
Navisence <sup>c</sup>	Zinal (Valais)	3	3.2	12	2019	crane-mounted net sampler	80
Avançon de Nant <sup>d</sup>	Les Plans-sur-Bex (Vaud)	4	1.3	10	2019/2020	manual basket sampler	55
Erlenbach <sup>e</sup>	Alpthal (Schwyz)	16	5.0	2	Since 2009	automatic basket sampler	122

140 <sup>a</sup> Gradient measured upstream of the SPG plates. At the Erlenbach, this gradient is the slope of the artificial approach flow channel  
 141 upstream of the SPG system.

142 <sup>b</sup> Depth-averaged mean flow velocities measured during the calibration measurements using an magnetic-inductive flow meter OTT MF  
 143 Pro (Albula and Navisence), a radar-based stage sensor Vegapuls WL 61 (Avançon de Nant), and a 2-D laser sensor TiM551 by SICK  
 144 AG© (Erlenbach)<sup>c</sup> More information on the sites is available in Nicollier et al. (2021).

145 <sup>d</sup> More information on the site is available in Antoniazza et al. (2022).

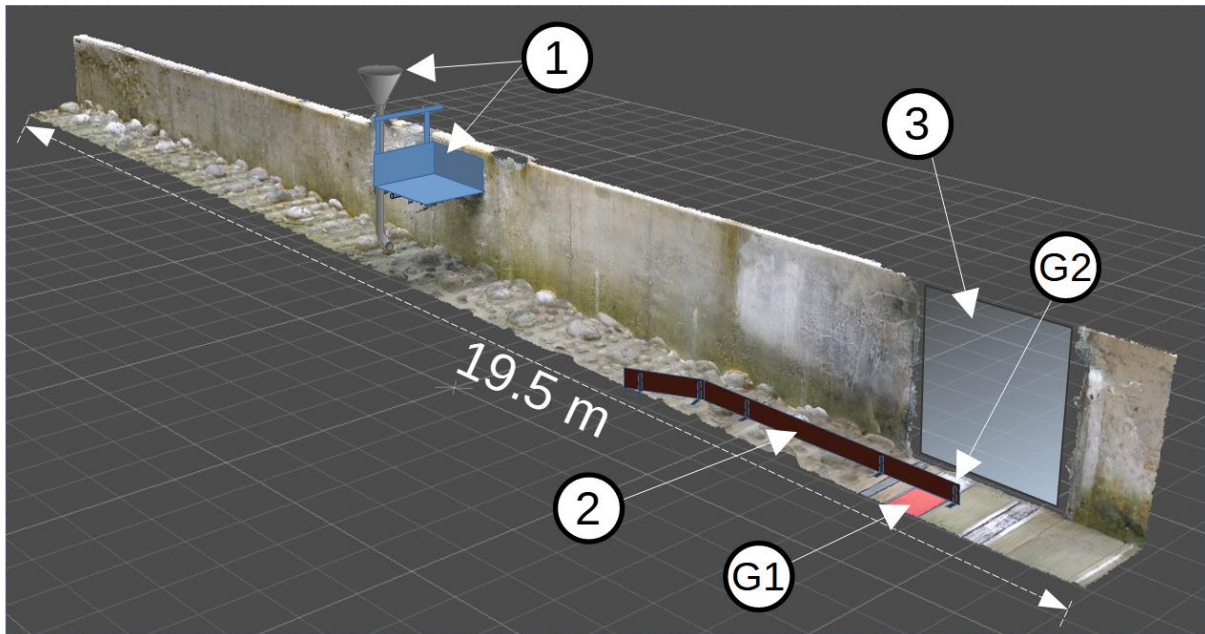
146 <sup>e</sup> More information on the site is available in e.g. Rickenmann et al. (2012), Wyss et al. (2016c), Rickenmann et al. (2018).

### 147 2.3 Controlled flume experiments

148 The first part of the signal conversion procedure described in this study is based on controlled flume experiments conducted  
 149 at the outdoor flume facility of the Oskar von Miller institute of TU Munich in Obernach, Germany. At this facility, we  
 150 reconstructed the bed characteristics of the Albula, Navisence and Avançon de Nant field sites, one after another, in a flume  
 151 test reach with dimensions of 24 m x 1 m equipped with two impact plates (Fig. 3). For each site reconstruction we tested  
 152 bedload material collected during field calibration measurements, and we adjusted the flow velocity, flow depth, and bed  
 153 roughness to match the respective field observations. A detailed description of the original flume setup and the performed  
 154 experiments can be found in Nicollier et al. (2020). In this paper, we primarily use the single-grain-size experiments  
 155 conducted in 2018 with the flume configured to match conditions at the Albula field site (Table 2). Single-grain-size  
 156 experiments consisted of feeding the flume with a fixed number of grains for each of the ten particle-size classes described in  
 157 Sect. 2.2 above. While these particles were transported over the SPG system, the full raw geophone signal was recorded. Up  
 158 to 33 repetitions were conducted until a representative range of amplitude and frequency values for each grain-size class was  
 159 obtained (Nicollier et al., 2021). The same procedure was repeated for two different flow velocities ( $V_f = 1.6 \text{ m s}^{-1}$  and  $2.4 \text{ m}$   
 160  $\text{s}^{-1}$ ). The obtained information was then used to derive empirical relationships between the mean particle size  $D_{m,j}$  and  
 161 properties of the SPG signal, as described in Sect. 2.5.2 below.

162 To illustrate the AF and AH methods and their respective performance, we use flume experiments that mimic the  
 163 Avançon de Nant field site, but with the addition of a 4 m wooden partition wall (Fig. 3) that shields one geophone plate  
 164 from impacting particles (Nicollier et al., 2022). With this modified setup, single-grain-size experiments were run using

165 grains from each of the 10 particle-size classes and originating from the Avançon de Nant channel, resulting in a total of 51  
 166 runs (Table 2). The flow velocity was set to  $3 \text{ m s}^{-1}$  to facilitate particle transport through the narrower flume section and is  
 167 therefore not representative for the Avançon de Nant site, where typical flow velocities were roughly  $1.3 \text{ m s}^{-1}$ .  
 168



169  
 170 **Figure 3:** Oblique view of the Obernach flume test reach with total length of 24 m and width of 1 m. The bed surface is paved with  
 171 particles with diameters equaling the characteristic  $D_{67}$  and  $D_{84}$  sizes of the natural beds of the reconstructed sites. Grains were  
 172 fed into the channel 8 m upstream from the SPG system location (G1 and G2) using either a vertical feed pipe or a tiltable basket  
 173 (1). The sensor plate G1 (in red) was shielded from direct particle impacts by the 4 m long removable partition wall (2). The  
 174 partition wall and the impact plates were decoupled from each other by a 2 mm vertical gap to prevent disturbances of the  
 175 recorded signal. Plexiglas walls (3) on each side of the flume facilitated video recordings of the experiments.

176  
 177 **Table 2:** Flume and hydraulic characteristics for the reconstruction of the Albula and the Avançon de Nant field sites.

Parameter	Units	Reconstructed field site setup	
		Albula (without partition wall)	Avaçon de Nant (with partition wall)
Flume width	m	1.02	1.02
Flume gradient of the natural bed	%	0.7	4.0
Bed surface $D_{67}$ <sup>a</sup>	mm	120	200
Bed surface $D_{84}$ <sup>a</sup>	mm	190	320
Number of $D_{67}$ -particles/m <sup>2</sup>	m <sup>-2</sup>	15.0	5.0
Number of $D_{84}$ -particles/m <sup>2</sup>	m <sup>-2</sup>	5.0	2.5
Min. water depth above SPG	m	0.79	0.35
Max. water depth above SPG	m	0.91	0.35
Min. flow velocity 10 cm above SPG <sup>b</sup>	m s <sup>-1</sup>	1.6	3.0
Max. flow velocity 10 cm above SPG <sup>b</sup>	m s <sup>-1</sup>	2.4	3.0
Min. unit discharge	m <sup>2</sup> s <sup>-1</sup>	1.6	0.8
Max. unit discharge	m <sup>2</sup> s <sup>-1</sup>	2.4	0.8
Number of different flow velocity settings	-	2	1

Total number of single-grain-size experiments	-	355	51
Total number of tested particles	-	10705	2485

178 <sup>a</sup> On the basis of line-by-number pebble counts at the natural site and a photo-sieving based granulometric analysis with BASEGRAIN  
179 software (Detert and Weitbrecht, 2013).  
180 <sup>b</sup> Flow velocities measured with the OTT MF Pro magnetic-inductive flow meter.

## 181 2.4 The amplitude-histogram method

182 Wyss et al. (2016a) introduced the packet-based amplitude-histogram (AH) method to derive grain-size information from  
183 geophone signals. A packet is defined as a brief interval, typically lasting 5 to 30 milliseconds, reflecting a single particle  
184 impact on a plate (Fig. 1b); it begins and ends when the signal envelope crosses a threshold amplitude of 0.0216 V. The  
185 signal envelope is computed in Python with the Hilbert transform (Jones et al., 2002), yielding the magnitude of the analytic  
186 signal, i.e. the total energy in the signal. Each packet's maximum amplitude is then used to assign it to a predefined  
187 amplitude class  $j$  delimited by amplitude-histogram thresholds  $th_{ah,j}$  (Table 3), yielding a packet-based amplitude histogram  
188 (e.g. Fig. 4 in Wyss et al., 2016a). Each amplitude class  $j$  is related to a corresponding grain-size class through the following  
189 relationship between the mean amplitude  $A_{m,j}$  [V] and the mean particle size  $D_{m,j}$  [mm]:

$$190 \quad A_{m,j} = 4.6 \cdot 10^{-4} \cdot D_{m,j}^{1.71}. \quad (1)$$

191 The coefficients in Eq. (1) were determined using 31 basket samples collected at the Erlenbach for which the maximum  
192 geophone amplitude was analyzed as a function of the B-axis of the largest particle found in the sample (Wyss et al., 2016a).  
193 The grain-size classes are delimited by the size of the meshes  $D_{sieve,j}$  used to sieve the bedload samples from field  
194 calibration measurements. For a given bedload sample, it is assumed that the number of packets between two amplitude-  
195 histogram thresholds  $th_{ah,j}$  is a good proxy for the fractional bedload mass between the respective sieve sizes (Wyss et al.,  
196 2016a). In the present study, we have extended the seven size classes used by Wyss et al. (2016a) to ten classes, in order to  
197 assess the performance of the AH and AF methods for larger particles.

198  
199 **Table 3: Characteristics of the size classes  $j$  according to Wyss et al. (2016a) with the sieve mesh sizes  $D_{sieve,j}$ , the mean particle  
200 diameter  $D_{m,j}$ , and the amplitude-histogram thresholds  $th_{ah,j}$  derived from Eq. (1). Additionally the lower and upper amplitude-  
201 frequency thresholds  $th_{af,low,j}$  and  $th_{af,up,j}$  derived from Eq. (4) and (5), respectively (see Sect. 2.5.2). The value of  $D_{m,j}$  for the  
202 largest class (10) in brackets is an estimate, because this size class is open-ended and thus the mean varied somewhat from site to  
203 site.**

Class $j$ [-]	$D_{sieve,j}$ [mm]	$D_{m,j}$ [mm]	$th_{ah,j}$ [V]	$th_{af,low,j}$ [V]	$th_{af,up,j}$ [V Hz <sup>-1</sup> ]
1	9.5	12.3	0.0216	0.0132	$1.55 \cdot 10^{-5}$
2	16.0	17.4	0.0527	0.0364	$2.33 \cdot 10^{-5}$
3	19.0	21.8	0.0707	0.0509	$4.45 \cdot 10^{-5}$
4	25.0	28.1	0.1130	0.0868	$7.67 \cdot 10^{-5}$
5	31.4	37.6	0.1670	0.1362	$1.78 \cdot 10^{-4}$
6	45.0	53.2	0.3088	0.2725	$3.93 \cdot 10^{-4}$
7	63.0	71.3	0.5489	0.5244	$7.05 \cdot 10^{-4}$
8	80.7	95.5	0.8378	0.8489	$1.56 \cdot 10^{-3}$
9	113.0	127.9	1.4919	1.6342	$2.79 \cdot 10^{-3}$
10	144.7	(171.5)	2.2760	2.6438	-

204

## 205 2.5 The amplitude-frequency method

206 In a recent study, Nicollier et al. (2022) showed that the SPG system is sensitive to extraneous particle impacts despite the  
207 isolating effect of the elastomer. Extraneous signals at individual geophone plates can arise from impacts occurring on  
208 neighboring plates, or from impacts on the concrete sill surrounding the SPG array. While attenuated to some extent, the  
209 elastic waves generated by such impacts can reach multiple geophone sensors with enough energy to be recorded as apparent  
210 packets. Thus, packet histograms (i.e. counts of the number of packets per class  $j$ ) are subject to a certain bias, especially in  
211 the lower size classes. The degree of bias was found to depend mainly on two factors. First, coarser grain sizes of transported  
212 bedload were shown to generate more apparent packets. Second, more apparent packets were recorded, for a given bedload  
213 mass, at transects containing more SPG plates. Nicollier et al. (2022) showed that packet characteristics such as the start  
214 time, the amplitude and the frequency help in identifying apparent packets and filtering them out from the final packet  
215 histograms. This filtering method was subsequently applied to all four field calibration datasets (Albula, Navisence, Avançon  
216 de Nant and Erlenbach) and helped to reduce the differences between the site-specific mean calibration relationships for the  
217 total bedload flux by about 30% (Nicollier et al., 2022). Based on these observations, the present study proposes an  
218 amplitude-frequency (AF) method as an adaptation of the amplitude-histogram (AH) method presented by Wyss et al.  
219 (2016a). By introducing two-dimensional (amplitude and centroid frequency) size class thresholds, the new method aims to  
220 reduce the effect of apparent packets and improve the accuracy of fractional bedload flux estimates. Note that the procedure  
221 does not allow to make the difference between particles impacting one plate simultaneously, but the high (10 kHz) recording  
222 frequency of the SPG system minimizes its probability of occurrence

### 223 2.5.1 Centroid frequency

224 According to the Hertz contact theory, the frequency at which a geophone plate vibrates is controlled by the size of the  
225 colliding particle (Johnson, 1985; Thorne, 1986; Bogen and Møen, 2003; Barrière et al., 2015; Rickenmann, 2017). In the  
226 present study, the frequency spectrum of a packet is characterized by the spectral centroid  $f_{\text{centroid}}$ . It represents the center of  
227 mass of the spectrum and is computed as

$$228 \quad f_{\text{centroid}} = \frac{\sum f_n \cdot A_{\text{FFT},n}}{\sum A_{\text{FFT},n}} \quad (2)$$

229 where  $A_{\text{FFT},n}$  [V·s] is the Fourier amplitude (computed with the Fast Fourier Transform FFT) corresponding to the frequency  
230  $f_n$  [Hz]. Following Wyss et al. (2016b), before applying the FFT, each packet is preprocessed in two steps. First, a cosine  
231 taper is applied at the edges of a max. 8 ms time window around the peak amplitude of each packet. Second, the signal  
232 contained in this time window is zero-padded on either side to reach an optimal number of sample points  $n_{\text{FFT}}$ . The taper is  
233 used to smooth the transition between the packet and the concatenated zeros, and to suppress spectral leakage, which results  
234 in a more accurate amplitude spectrum. The value of  $n_{\text{FFT}}$  was set to  $2^7$  in order to adequately resolve the amplitude  
235 spectrum of the raw signal contained in the max. 8 ms time window. This time window focuses on the first arrival waveform  
236 to obtain a more accurate evaluation of the high-frequency content of the packet (Nicollier et al., 2022). The single-sided  
237 Fourier transform of the processed packet is then computed in order to extract  $A_{\text{FFT}}$  and derive  $f_{\text{centroid}}$  (Eq. 2). A decrease  
238 in  $f_{\text{centroid}}$  with increasing particle size was observed for different bedload surrogate monitoring techniques (Belleudy et al.,  
239 2010; Uher and Benes, 2012; Barrière et al., 2015). Furthermore,  $f_{\text{centroid}}$  has the advantage of showing weaker dependency  
240 on the flow velocity and transport mode than the maximum registered packet amplitude (Wyss et al. 2016b; Chen et al.,  
241 2022). As shown by Nicollier et al. (2022),  $f_{\text{centroid}}$  also contains information about the impact location of a packet-  
242 triggering particle. Because high frequencies are more rapidly attenuated than low frequencies along the travel path of a



243 seismic wave, (apparent) packets triggered by impacts on a given plate typically have higher  $f_{\text{centroid}}$  values than packets  
 244 triggered by impacts occurring beyond that plate's boundaries.

## 245 2.5.2 Flume-based amplitude-frequency thresholds

246 The particle mass associated with an individual signal packet is strongly dependent on the size of the impacting particle.  
 247 Inferring sediment transport rates from SPG signals thus requires assigning each packet to a corresponding sediment size  
 248 class using threshold values of packet characteristics (Table 3). Wyss et al. (2016a) derived size class thresholds (or AH  
 249 thresholds) of packet peak amplitude from field measurements (Eq. 1). In the present study, we take advantage from the  
 250 single-grain-size experiments conducted at the flume facility (without the partition wall) (Nicollier et al., 2021) to derive  
 251 size class thresholds combining packet amplitude and frequency (or AF thresholds). Each packet is assigned to a given  
 252 class  $j$  delimited by a lower threshold  $th_{af,low,j}$  based on the maximum amplitude of the packet's envelope  $MaxAmp_{env}$  [V],  
 253 and an upper threshold  $th_{af,up,j}$  based on the ratio  $MaxAmp_{env}/f_{\text{centroid}}$  [V Hz<sup>-1</sup>]. Compared to the raw signal, the envelope  
 254 has the advantage of returning the magnitude of the analytical signal and thus better outlines the waveform by omitting the  
 255 harmonic structure of the signal (Fig. 2b). Similar combinations of amplitude and frequency have been used to infer particle  
 256 sizes and improve the detectability of bedload particles in previous studies involving impact plates (Tsakiris et al., 2014;  
 257 Barrière et al., 2015; Wyss et al., 2016b; Koshiba and Sumi, 2018) and pipe hydrophones (Choi et al., 2020).

258 The lower and upper amplitude-frequency thresholds are obtained as follows. First, all packets recorded during the  
 259 single-grain-size experiments are filtered with respect to the following criterion adapted from Nicollier et al. (2022):

$$260 \quad \text{Criterion: } f_{\text{centroid}} > a_c \cdot e^{(b_c \cdot MaxAmp_{env})}, \quad (3)$$

261 with  $a_c = 1980$  Hz and  $b_c = -1.58$  V<sup>-1</sup>. The values for the linear coefficient  $a_c$  and the exponent  $b_c$  were obtained through an  
 262 optimization process discussed below (Sect. 4.1), and were found to ideally set apparent packets apart from real ones.  
 263 Packets that do not meet this criterion are considered as apparent packets and are ignored in the further analysis in order to  
 264 obtain more accurate threshold values. Note that in the present study the criterion in Eq. 3 has not been applied to the data  
 265 when implementing the AH method developed by Wyss et al. (2016a).

266 The next step consists in fitting a power-law least-squares regression line through the 75<sup>th</sup> percentile amplitude  
 267  $MaxAmp_{env,75th,j}$  and amplitude-frequency  $(MaxAmp_{env}/f_{\text{centroid}})_{75th,j}$  values of the packets detected for a given grain-  
 268 size class  $j$  fed into the flume that met the filtering criterion (Fig. 4), resulting in the following two equations:

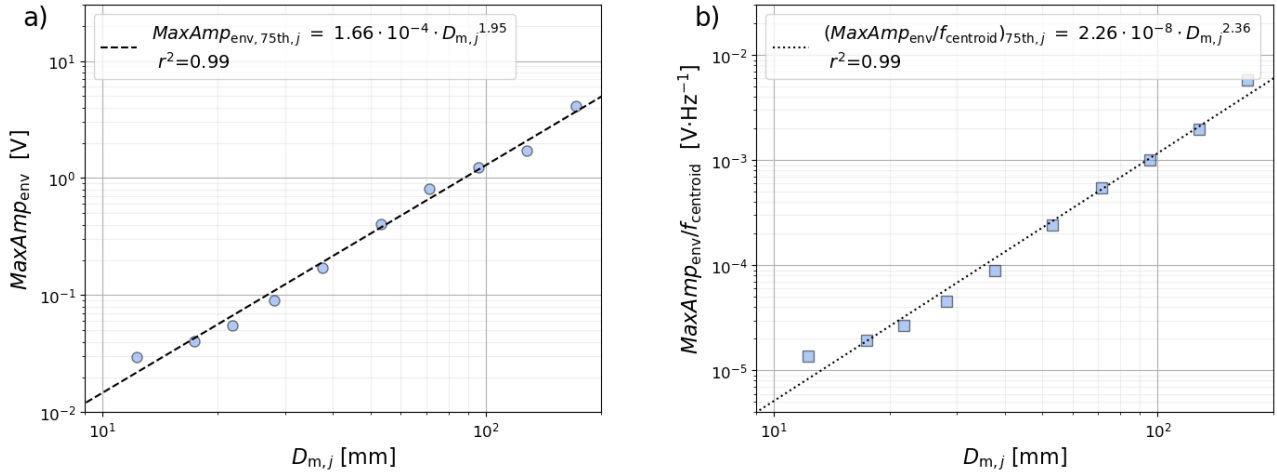
$$269 \quad MaxAmp_{env,75th,j} = 1.66 \cdot 10^{-4} \cdot D_{m,j}^{1.95}, \quad \text{and} \quad (4)$$

$$270 \quad \left( \frac{MaxAmp_{env}}{f_{\text{centroid}}} \right)_{75th,j} = 2.26 \cdot 10^{-8} \cdot D_{m,j}^{2.36}. \quad (5)$$

271 Finally, the lower threshold values  $th_{af,low,j}$  are obtained by replacing  $D_{m,j}$  in Eq. (4) with the lower sieve sizes  
 272  $D_{\text{sieve},j}$ , while the upper threshold values  $th_{af,up,j}$  are obtained by replacing  $D_{m,j}$  in Eq. (5) with the upper sieve sizes  
 273  $D_{\text{sieve},j+1}$  (Table 3 and triangles in Fig. 5). The advantage in fitting functions such as Eq. (4) and (5) is that they allow the  
 274 computation of thresholds for any classification of particle (sieve) sizes.

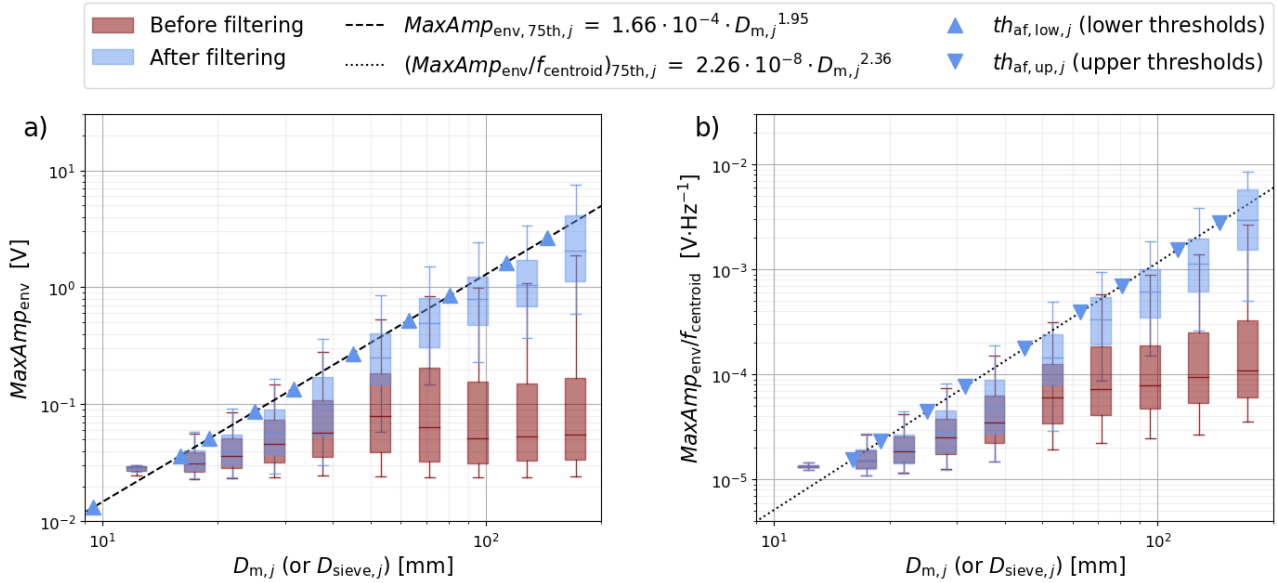
275 Particularly for the largest particles, apparent packets can greatly outnumber real packets. Due to their relatively small  
 276 amplitudes, these apparent packets can substantially dilute the average signal response associated with the largest grain sizes  
 277 (see the red boxplots in Fig. 5). However, filtering out apparent packets reveals a clear relationship, which would otherwise  
 278 be obscured, between the mean particle size  $D_{m,j}$  and both the amplitude  $MaxAmp_{env}$  and the ratio  $MaxAmp_{env}/f_{\text{centroid}}$

279 (see the blue boxplots in Fig. 5). Overall, the filtering with criterion (Eq. 3) at the Obernach flume site eliminated about 61%  
 280 of all the packets.



281  
 282 **Figure 4: Power-law least-squares regression relationships between the mean particle diameter  $D_{m,j}$  and the 75<sup>th</sup> percentile of the**  
 283 **(a) amplitude  $MaxAmp_{env,75th,j}$  and (b) amplitude-frequency  $(MaxAmp_{env}/f_{centroid})_{75th,j}$  values obtained from the single-grain-size**  
 284 **experiments after filtering out apparent packets using the filtering criterion in Eq. (3).**

285



286  
 287 **Figure 5: Range of signal responses obtained for each individual grain-size class fed into the flume before (red boxes) and after**  
 288 **(blue boxes) filtering out apparent packets using the filtering criterion in Eq. (3), with (a) the maximum amplitude of the envelope**  
 289  **$MaxAmp_{env}$  and (b) the ratio  $MaxAmp_{env}/f_{centroid}$  as functions of the mean particle diameter  $D_{m,j}$ . In (a), the lower threshold**  
 290 **values  $th_{af,low,j}$  are obtained by replacing  $D_{m,j}$  with the lower sieve sizes ( $D_{sieve,j}$ ) in the equation of the dashed power-law regression**  
 291 **line (Eq. 4). In (b), the upper threshold values  $th_{af,up,j}$  are obtained by replacing  $D_{m,j}$  with the upper sieve sizes ( $D_{sieve,j+1}$ ) in the**  
 292 **equation of the dotted power-law regression line (Eq. 5).**

### 293 2.5.3 Application to field calibration measurements

294 The lower and upper thresholds  $th_{af,low,j}$  and  $th_{af,up,j}$  obtained from the filtered flume experiments can be transferred to the  
 295 field calibration datasets, if the SPG apparatus and the geophone data recording and preprocessing routines are identical in

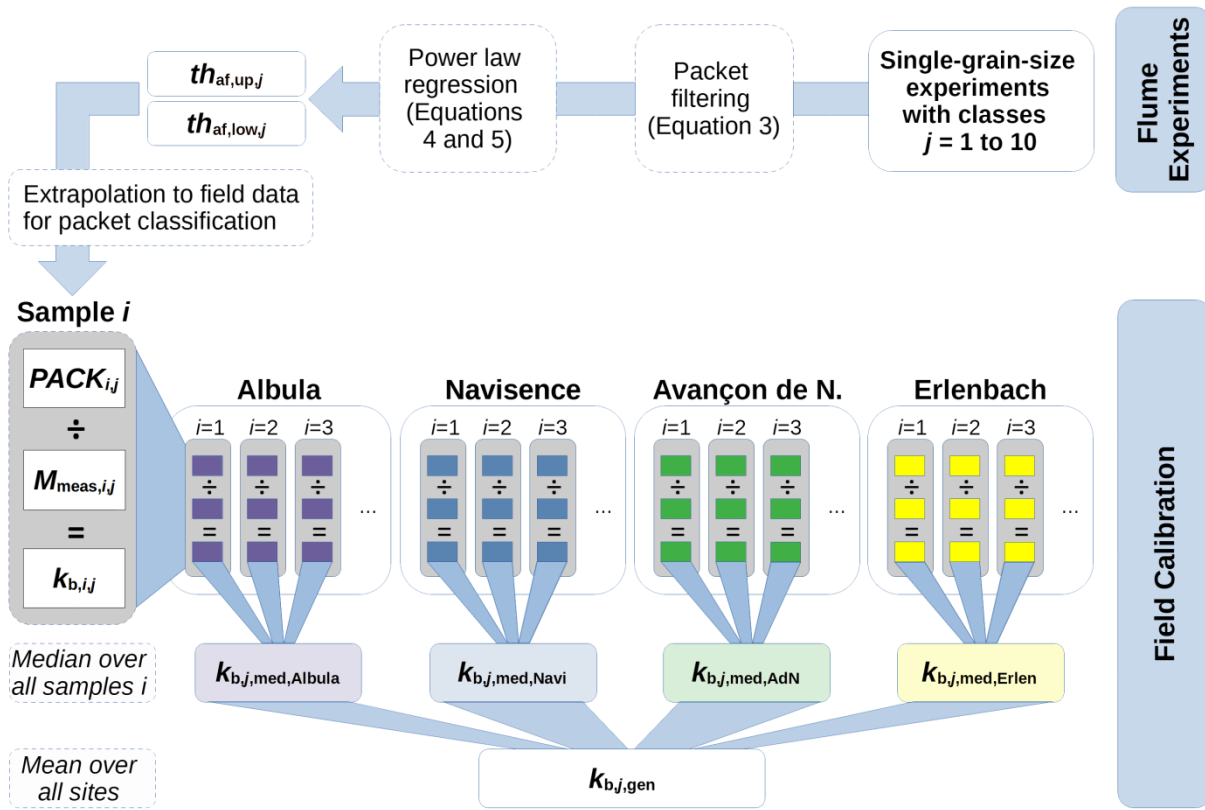
296 both cases. The following steps will now lead us to the final general calibration coefficients  $k_{b,j,gen}$  (Fig. 6). First, for each  
 297 field measurement  $i$ , the thresholds  $th_{af,low,j}$  and  $th_{af,up,j}$  are used for counting the number of packets per class  $j$  from the  
 298 recorded geophone signal. Second, a sample- and class-specific calibration coefficient  $k_{b,i,j}$  with units  $[kg^{-1}]$  is obtained by  
 299 dividing the number of recorded packets  $PACK_{i,j}$  by the sampled fractional mass  $M_{meas,i,j}$  as follows:

$$300 \quad k_{b,i,j} = \frac{PACK_{i,j}}{M_{meas,i,j}}. \quad (6)$$

301 Finally, the general calibration coefficient  $k_{b,j,gen}$  is computed for each class  $j$  using

$$302 \quad k_{b,j,gen} = \frac{1}{N_{stations}} \sum_{stations} k_{b,j,med,station}, \quad (7)$$

303 where  $k_{b,j,med,station}$  is the site-specific median calibration coefficient computed over all samples  $i$ , and  $N_{stations}$  is the  
 304 number of stations. Even though the number of calibration measurements differs from site to site, each coefficient  
 305  $k_{b,j,med,station}$  in Eq. (7) is equally weighted in order to give the same importance to site-specific factors possibly affecting  
 306 the signal response at each site.



307  
 308 **Figure 6: Workflow leading from the single-grain-size flume experiments with particles from ten size classes  $j$  (top right) to the**  
 309 **final array of general calibration coefficients  $k_{b,j,gen}$ . Central elements are the lower and upper threshold values  $th_{af,low,j}$  and**  
 310  **$th_{af,up,j}$ , the number of recorded packets  $PACK_{i,j}$  per sample  $i$  and class  $j$ , the sampled fractional mass  $M_{meas,i,j}$ , the sample- and**  
 311 **class- specific calibration coefficient  $k_{b,i,j}$ , and finally the site-specific median calibration coefficient  $k_{b,j,med,station}$ . To enable a**  
 312 **comparison with the AH method developed by Wyss et al. (2016a), the “Field Calibration” part of the workflow was also carried**  
 313 **out with the AH thresholds  $th_{ah,j}$  (see Table 3).**

314 At this point, the single array of calibration coefficients  $k_{b,j,gen}$  is applied as follows to each field calibration  
 315 measurement  $i$  in order to obtain fractional bedload mass estimates  $M_{est,i,j}$ :

316 
$$M_{est,i,j} = k_{b,j,gen} \cdot PACK_{i,j} . \quad (8)$$

317 Rickenmann and Fritschi (2017) showed that bedload mass estimates derived from SPG measurements are more accurate at  
 318 higher transport rates. The estimated fractional bedload mass  $M_{est,i,j}$  can be converted to a unit fractional transport rate  
 319  $q_{b,est,i,j}$  [ $\text{kg m}^{-1} \text{s}^{-1}$ ] using:

320 
$$q_{b,est,i,j} = \frac{1}{w_p \cdot n_p} \cdot \frac{M_{est,i,j}}{\Delta t_i} , \quad (9)$$

321 where  $w_p$  is the standard width of an impact plate (0.5 m),  $n_p$  is the number of plates (which may include the whole transect,  
 322 or a section of particular interest), and  $\Delta t_i$  is the sampling duration in seconds. Finally, the estimated unit total bedload flux  
 323  $q_{b,tot,est,i}$  can be computed as follows:

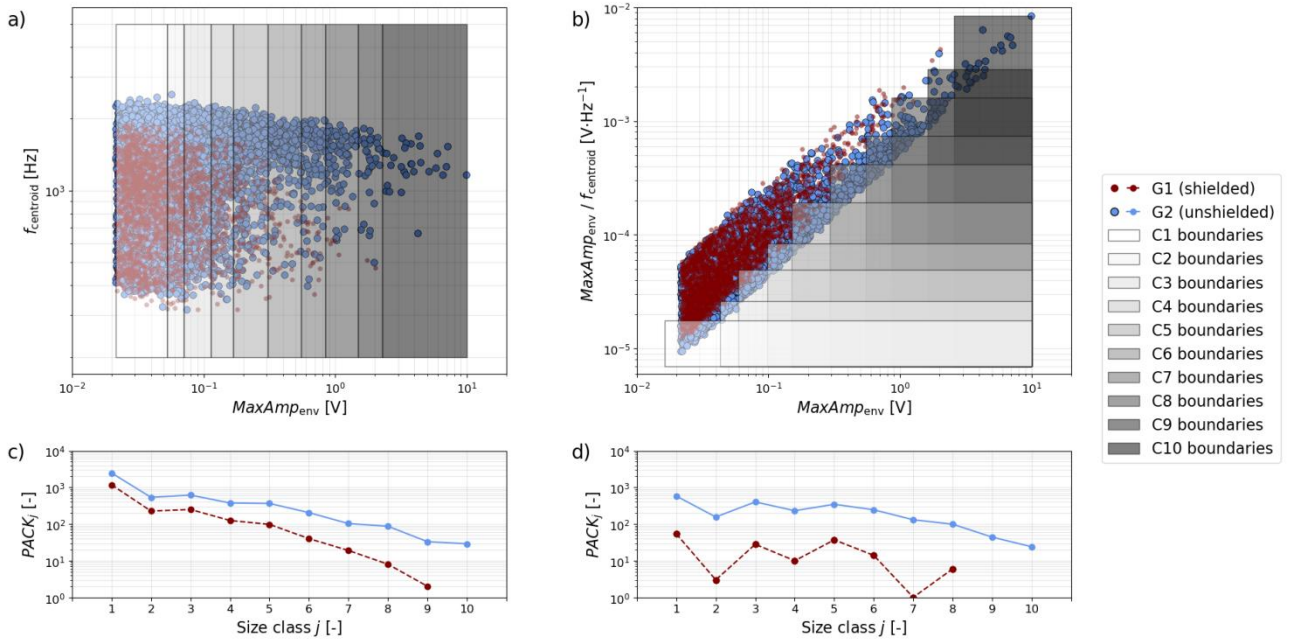
324 
$$q_{b,tot,est,i} = \sum_{j=1}^{10} q_{b,est,i,j} \quad (10)$$

325 Note that the exact same procedure was followed using the AH thresholds  $th_{ah,j}$  derived from Wyss et al. (2016a) (Eq. 1;  
 326 Table 3) to compare the performance between the AH method and the new AF method.

### 327 **3 Results**

#### 328 **3.1 Flume experiments**

329 The flume experiments performed in the modified Avançon de Nant setup with the partition wall help to illustrate the two  
 330 calibration methods. Fig. 7a and 7b show the amplitude and frequency characteristics of all packets detected by the SPG  
 331 system during these experiments. Packets detected by the shielded sensor G1 all originate from impacts that occurred either  
 332 on the concrete bed or on plate G2 (Nicollier et al., 2022). Packets detected by the unshielded sensor G2 are considered as  
 333 apparent if they are located in the area of the amplitude-frequency graph (Fig. 7a) where G1 and G2 packets overlap. Such  
 334 packets are presumed to have been triggered by impacts on the concrete bed too. This overlapping area arises from the fact  
 335 that a seismic wave generated by an impact on the concrete bed follows a similar path towards both sensors, resulting in the  
 336 recording of two apparent packets with comparable characteristics. The remaining packets, detected by G2 and located in the  
 337 non-overlapping area of the amplitude-frequency graph, are considered as real, rather than apparent. The difference in  
 338  $f_{centroid}$  between real and apparent packets (Fig. 7a) reflects the faster attenuation of higher frequencies during wave  
 339 propagation, as mentioned earlier. Size class boundaries derived by the AH method of Wyss et al. (2016a) encompass all of  
 340 the packets, both apparent and real (Fig. 7a). This is because the boundaries are defined solely by AH thresholds ( $th_{ah,j}$ ). By  
 341 contrast, in the AF method proposed here, the two-dimensional class boundaries given by  $th_{af,low,j}$  and  $th_{af,up,j}$  cover only a  
 342 fraction of all detected packets (Fig. 7b). Applying the step-like AF thresholds leads to a strong reduction of the number of  
 343 packets  $PACK_j$  within each size class  $j$  for plate G1 (shielded), particularly for the smaller classes. Meanwhile, the AF  
 344 thresholds had little effect on the number of detected packets for G2 (unshielded), except for a strong decrease for classes  $j =$   
 345  $1$  and  $2$ , and a slight increase for classes  $j = 6$  to  $10$  (Fig. 7c and 7d). The AH thresholds encompass in total 1945 packets for  
 346 the shielded geophone G1, and 4823 packets for the unshielded geophone plate G2. In comparison, the AF thresholds  
 347 encompass in total 159 packets for the shielded geophone G1, and 2202 packets for the unshielded geophone plate G2  
 348 (counting the packets in the overlapping class boundaries only once). Considering apparent packets as noise and real packets  
 349 as signal, applying the new AF method results in an increased signal to noise ratio, as shown by the larger vertical separation  
 350 between the blue (signal) and red (noise) lines in Fig. 7d compared to Fig. 7c.

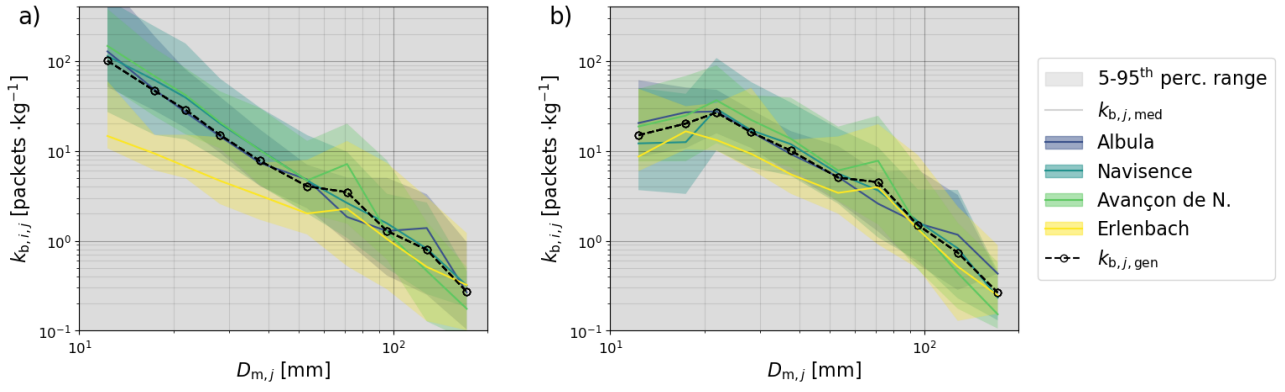


351

352 **Figure 7: Characteristics of the packets recorded during single-grain-size experiments conducted with the Avançon de Nant flume**  
 353 **setup using the partition wall, with the maximum amplitude of the envelope  $MaxAmp_{env}$  and the centroid frequency  $f_{centroid}$ . The**  
 354 **red and blue dots correspond to packets recorded by the shielded plate G1 and the unshielded plate G2, respectively. The grey**  
 355 **rectangles are the class boundaries delimited by the thresholds obtained for the AH method (a) and the AF method (b). The**  
 356 **number of packets  $PACK_j$  located within the class boundaries delimited by the AH thresholds and the AF thresholds are indicated**  
 357 **in (c) and (d), respectively. In (a),  $f_{centroid}$  is shown as function of  $MaxAmp_{env}$  for information purposes only.**

### 358 3.2 Field calibration coefficients

359 As discussed in the previous section, the number of packets  $PACK_{i,j}$  detected for a given class  $j$  varies together with the  
 360 thresholds  $th_{ah,j}$ ,  $th_{af,low,j}$  and  $th_{af,up,j}$ . Because the measured fractional bedload mass  $M_{meas,i,j}$  remains constant, the  
 361 calibration coefficients  $k_{b,i,j}$  will depend on the number of packets detected, and thus on the thresholds that are used to  
 362 classify them. We can make the following observations regarding the calibration coefficients  $k_{b,i,j}$  obtained using the AF  
 363 method (Fig. 8b) compared to the AH method (Fig. 8a). First, the  $k_{b,i,j}$  coefficients of the smaller size classes are  
 364 substantially lower, meaning that fewer packets per unit mass are detected. Second, for the larger size classes, slightly more  
 365 packets are detected per unit mass. Third, the overall scatter of the  $k_{b,i,j}$  coefficients across all sites is smaller, in particular  
 366 for the six smallest classes  $j$ . This is reflected in the decrease of the mean coefficient of variation (CV) across all classes  $j$   
 367 and all sites from  $CV = 1.17$  (in the AH method) to  $CV = 0.93$  (in the AF method). Fourth, the scatter of the site-specific  
 368  $k_{b,i,j}$  coefficients is usually smaller. This is supported by the change of the mean CV across all classes from 0.89 to 0.54 for  
 369 the Albul, from 0.83 to 0.75 for the Avançon de Nant and from 1.31 to 1.00 for the Erlenbach, between the AH and AF  
 370 methods. The mean CV for the Navisence site however remains unchanged at 0.85. The general coefficients  $k_{b,j,gen}$  obtained  
 371 from the site-specific median coefficients  $k_{b,j,med}$  using Eq. (7) are listed in Table 4.



372

373

374

375

376

**Figure 8:** The  $k_{b,i,j}$  calibration coefficients obtained with the AH method (a) and the AF method (b) for each field site. The colored areas indicate the range between the 5<sup>th</sup> and the 95<sup>th</sup> percentile  $k_{b,i,j}$  values, the full lines indicate the site-specific median coefficients  $k_{b,j,med}$  and the black dashed lines indicate the final general calibration coefficients  $k_{b,j,gen}$  as a function of the mean particle diameter  $D_{m,j}$  of each grain-size class  $j$ .

377

378

379

**Table 4:** General calibration coefficients  $k_{b,j,gen}$  obtained for each grain-size class  $j$  with the AH method and the AF method using Eq. (7).

	Method	Units	$j = 1$	$j = 2$	$j = 3$	$j = 4$	$j = 5$	$j = 6$	$j = 7$	$j = 8$	$j = 9$	$j = 10$
$k_{b,j,gen}$	AH	$\text{kg}^{-1}$	100.67	46.43	28.68	15.03	7.76	4.04	3.47	1.29	0.79	0.27
	AF	$\text{kg}^{-1}$	14.97	20.15	26.65	16.15	10.06	5.05	4.49	1.50	0.74	0.27

380

381

### 3.3 Bedload flux estimates

382

383

384

385

386

387

388

389

390

391

392

393

394

We can now insert the general calibration coefficients  $k_{b,j,gen}$  in Eq. (8) to compute fractional bedload mass estimates  $M_{est,i,j}$  and subsequently the unit fractional flux estimates  $q_{b,est,i,j}$  (Eq. 9) for every sample collected at the four field sites. Fig. 9 illustrates the accuracy of the bedload flux estimates obtained with the AF method for each sample across the grain-size classes and the field sites. The results obtained with the AH method can be found in Supplementary Information S3, and Table 5 provides further information on the performance of the two methods. The dashed colored power-law regression lines shown in Fig. 9, described by the corresponding linear coefficient  $a$  and exponent  $b$  (Table 5), indicate possible trends in over/under-estimation at each field site. The coefficient of determination  $R^2$  describes the accuracy of the estimates relative to the 1:1 line. The root-mean-square error ( $RMSE$ ) quantifies the expected error of the estimates and is expressed in [ $\text{kg m}^{-1} \text{s}^{-1}$ ]. When applied to the field calibration data, the AF method generally yields more accurate flux estimates than the AH method does. This is most notably reflected by the  $R^2$  values and the percentages  $p_{factor\_2}$  and  $p_{factor\_5}$  of all detected samples whose estimated bedload fluxes differ by less than a factor of 2 and 5, respectively, from the measured values (Table 5). The five smallest grain-size classes were most strongly affected by these improvements, whereas the estimates for the largest fractions ( $j = 7$  to 10) were only slightly improved.

395

396

397

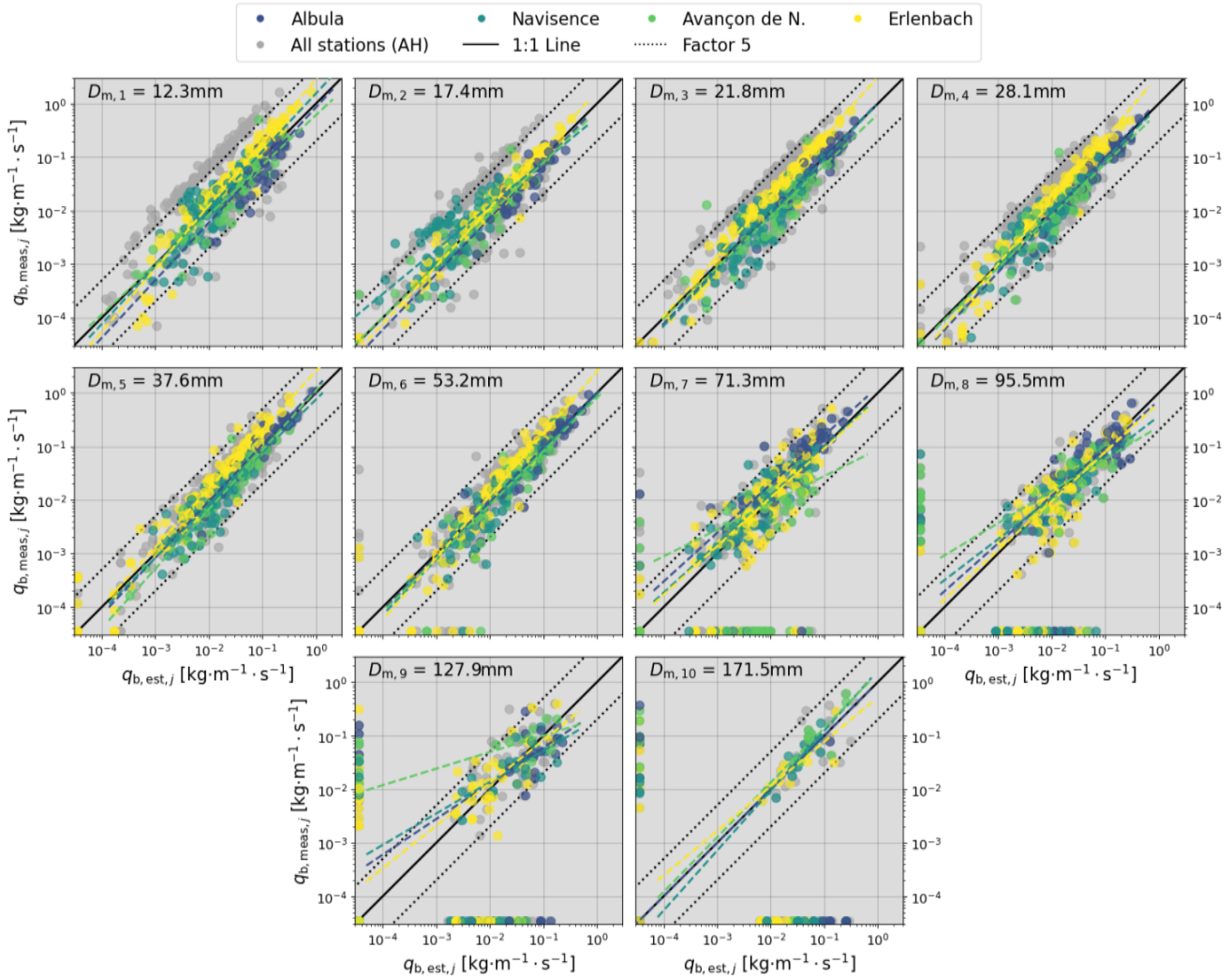
398

399

Aside from these comparative observations, it is also worth mentioning the following more general findings that are valid for both methods: (i) for most size fractions, the relative scatter of the estimates (on the log-log plots) decreases with increasing transport rates; (ii) at low transport rates, mass fluxes are generally overestimated, while at high transport rates they are generally underestimated; (iii) mass fluxes for the Erlenbach closely follow the 1:1 line but tend to be slightly underestimated; (iv) the number of measured ( $N_{samples,meas}$ ) and estimated ( $N_{samples,est}$ ) samples both decrease with

400 increasing particle size. Samples for which either the measured or the estimated flux equals 0 are indicated as dots along the  
 401 axes in Fig. 9. If the measured flux is zero but the estimated flux is positive, the sample can be regarded as false positive  
 402 (Fawcett, 2006). The difference between  $N_{\text{samples,meas}}$  and  $N_{\text{samples,est}}$  in Table 5 indicates that the occurrence of such false  
 403 positive samples increases with increasing particle size. Further performance metrics derived from the confusion matrix can  
 404 be found in the Supporting Information (Table S2).

405



406

407 **Figure 9: Unit fractional transport rate estimates obtained with the AF method for each size class  $j$  and each station. The light grey**  
 408 **dots in the background indicate the estimates obtained with the AH method and are represented in more detail in the Supporting**  
 409 **Information (Fig. S1). Each frame is annotated with the mean particle size  $D_{m,j}$  of the represented class. The solid black lines**  
 410 **correspond to the reference 1:1 line while the dotted lines delimit factors of 5 above and below (from 0.2 to 5). The dashed colored**  
 411 **lines are power-law regression lines; the mean coefficients over all four sites are listed in Table 5. The dots along the axes indicate**  
 412 **samples for which either the measured or the estimated unit fractional flux equals 0. These samples are not considered for the**  
 413 **computation of the trend lines.**

414

415 **Table 5: Performance of the AH method and the AF method regarding fractional flux estimates for each class  $j$  with following**  
 416 **parameters: the linear coefficient  $a$ , the exponent  $b$  and the correlation coefficient  $r$  of the power-law regression lines visible in Fig.**  
 417 **9; the coefficient of determination  $R^2$ ; the root-mean-square error  $RMSE$ ; and the percentage of all detected samples for which the**  
 418 **estimated value differs from the measured value by less than a factor of 2 and 5  $p_{\text{factor}_2}$  and  $p_{\text{factor}_5}$ , respectively. These values**

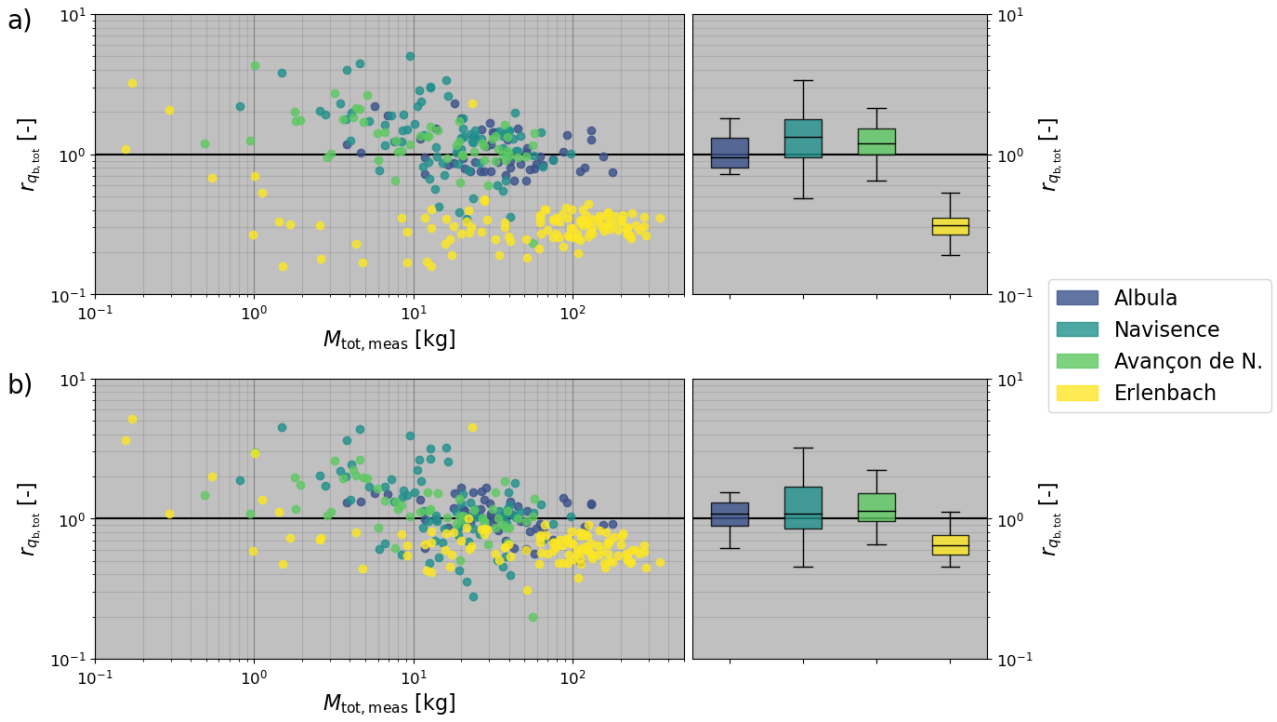
419 were first computed for each site separately and then averaged over all four sites. The number of measured  $N_{\text{samples,meas}}$  and the  
 420 number of estimated samples  $N_{\text{samples,est}}$  showing a positive unit fractional rate were summed over all four sites.

		Units	$j = 1$	$j = 2$	$j = 3$	$j = 4$	$j = 5$	$j = 6$	$j = 7$	$j = 8$	$j = 9$	$j = 10$
$N_{\text{samples,meas}}$		-	308	308	306	306	302	287	240	213	112	53
AH method	$N_{\text{samples,est}}$	-	308	305	307	301	299	289	267	237	149	117
	$r$	-	0.77	0.83	0.87	0.88	0.91	0.89	0.73	0.75	0.53	0.46
	$a$	-	3.6	2.02	1.95	2	1.39	1.54	0.85	0.53	0.42	0.58
	$b$	-	0.94	0.95	1	1.05	1.01	1.05	0.83	0.83	0.64	0.6
	$R^2$	-	0.4	0.51	0.64	0.70	0.78	0.81	0.36	0.57	-0.16	0.11
	$RMSE$	$\text{kg} \cdot \text{m}^{-1} \cdot \text{s}^{-1}$	0.094	0.031	0.044	0.036	0.052	0.048	0.038	0.037	0.04	0.06
	$p_{\text{factor}_2}$	%	50	54	54	58	64	72	50	58	37	57
	$p_{\text{factor}_5}$	%	72	84	92	93	96	95	86	81	68	73
AF Method	$N_{\text{samples,est}}$	-	308	305	307	305	301	295	279	242	161	84
	$r$	-	0.79	0.82	0.89	0.91	0.93	0.93	0.81	0.78	0.52	0.61
	$a$	-	1.46	0.96	1.44	1.54	1.41	1.3	0.73	0.49	0.3	1.16
	$b$	-	1.07	0.98	1.03	1.05	1.06	1.05	0.81	0.79	0.59	0.74
	$R^2$	-	0.71	0.72	0.8	0.84	0.85	0.83	0.42	0.55	-0.08	0.59
	$RMSE$	$\text{kg} \cdot \text{m}^{-1} \cdot \text{s}^{-1}$	0.068	0.021	0.035	0.027	0.045	0.040	0.035	0.039	0.042	0.061
	$p_{\text{factor}_2}$	%	69	74	69	78	75	81	53	58	43	47
	$p_{\text{factor}_5}$	%	96	93	98	98	97	97	91	83	68	56

421

422 As indicated by Eq. (10), the unit total flux estimates are computed as the sum of the unit fractional flux estimates over  
 423 all 10 classes. Fig. 10 shows the ratio  $r_{q_{b,\text{tot}}}$  between the estimated total flux  $q_{b,\text{tot,est}}$  and the measured total flux  $q_{b,\text{tot,meas}}$   
 424 for all 308 calibration samples, as a function of the sampled total mass  $M_{\text{tot,meas}}$ . Here, the estimates for the Albula, the  
 425 Navisence and the Avançon de Nant sites are slightly more accurate with the AF method than with the AH method, whereas  
 426 the estimates for the Erlenbach improve substantially, with the median  $r_{q_{b,\text{tot}}}$  value increasing from 0.31 to 0.64. Note that  
 427 the observations (i) to (iii) made earlier regarding the fractional flux estimates are also valid here. Fig. 10 also provides an  
 428 interesting overview of the sampled masses at all four stations, reflecting the capacities of the different devices (automated  
 429 and manual basket samplers and crane-mounted net sampler) used to collect the calibration samples.



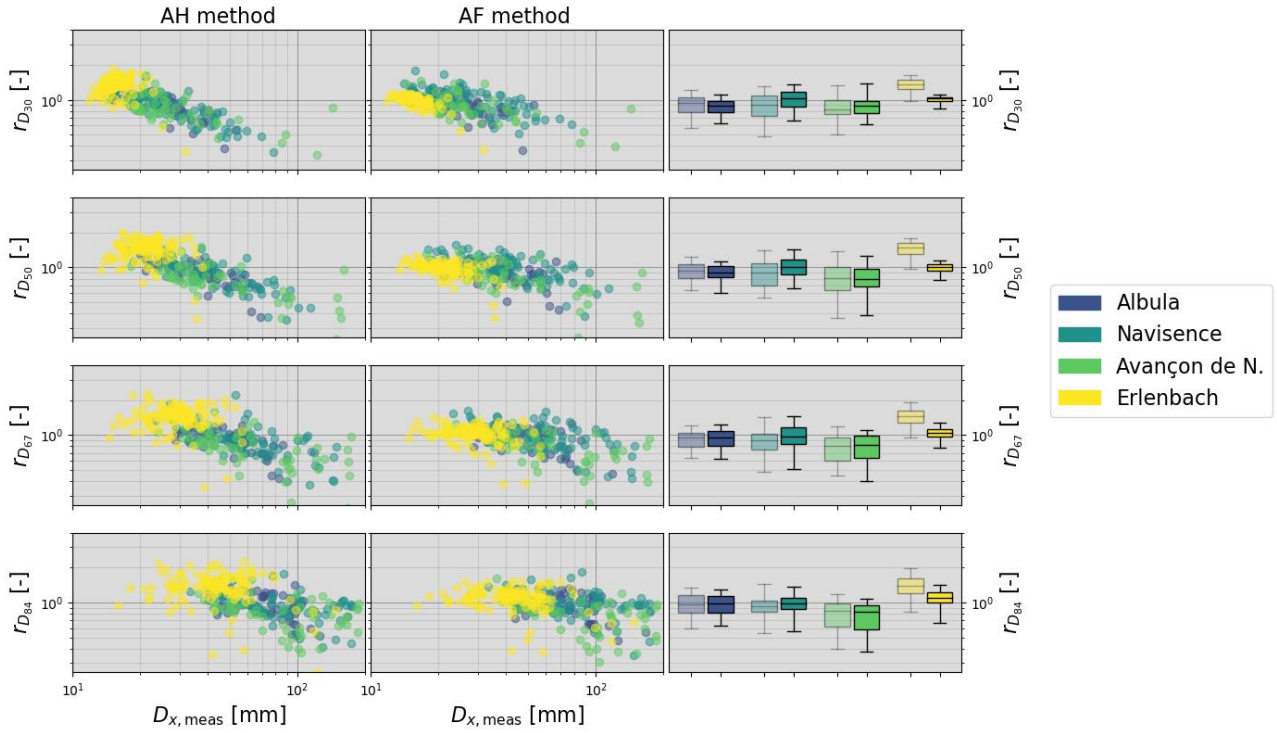


430

431 **Figure 10: Ratio  $r_{q_{b,tot}}$  between the estimated and the measured unit total mass flux as a function of the total sampled mass**  
 432  **$M_{tot,meas}$ , for each collected sample  $i$  and each station, for the AH method (a) and the AF method (b). The boxplots on the right**  
 433 **indicate the range of  $r_{q_{b,tot}}$  values obtained for each station.**

### 434 3.4 Grain-size estimates

435 We can combine the SPG bedload flux estimates for all grain-size fractions and thus derive grain-size distributions, which  
 436 can then be compared to the measured size distributions of each calibration sample. Fig. 11 compares the performance of the  
 437 AH and the AF methods in estimating the characteristic grain sizes  $D_{30}$ ,  $D_{50}$ ,  $D_{67}$  and  $D_{84}$  (where  $D_x$  is the grain diameter for  
 438 which  $x$  percent of the sampled bedload mass is finer). The accuracy of the estimates is indicated by the ratio  $r_{D_x}$  between the  
 439 estimated and the measured characteristic grain size  $D_x$ . Compared to the AH method, the AF method mainly improves the  
 440 estimates of the four characteristic grain sizes for the Navisence and the Erlenbach sites, but has little effect at the other two  
 441 sites. The largest improvement is achieved for the Erlenbach site, with the median  $r_{D_{30}}$  changing from 1.37 to 1.02, the  
 442 median  $r_{D_{50}}$  changing from 1.48 to 1.01, the median  $r_{D_{67}}$  changing from 1.46 to 1.05 and the median  $r_{D_{84}}$  changing from  
 443 1.39 to 1.10. The overall accuracy of the estimates decreases with increasing characteristic size  $D_x$  for both methods, and for  
 444 every characteristic size  $D_x$ , the  $D_x$  tends to be overestimated for finer grain mixtures and underestimated for coarser grain  
 445 mixtures.



446

447 **Figure 11: Ratio  $r_{D_x}$  between the estimated and the measured characteristic grain sizes  $D_{30}$ ,  $D_{50}$ ,  $D_{67}$  and  $D_{84}$  as a function of the**  
 448 **measured grain diameter  $D_{x, meas}$  for each collected sample  $i$  and each station using the AH method (column 1) and the AF method**  
 449 **(column 2).  $D_x$  is the grain diameter for which  $x$  percent of the sampled bedload is finer. The boxplots in column 3 indicate the**  
 450 **range of  $r_{D_x}$  values obtained for each station. The boxes in faded colors show the results obtained with the AH method and the**  
 451 **boxes in brighter colors show the results obtained with the AF method.**

452

## 4 Discussion

453

### 4.1 The hybrid calibration procedure

454

Recent studies have pointed out the difficulty of transferring flume-based calibrations of the impact plate system to field applications (e.g. Mao et al., 2016; Wyss et al., 2016c; Kuhnle et al., 2017). In the hybrid calibration approach presented here, we took advantage of controlled flume experiments to obtain amplitude and amplitude-frequency thresholds for each particle-size class, which were subsequently applied to field calibration datasets to derive the general calibration coefficients  $k_{b,j,gen}$ .

459

The entire hybrid calibration procedure was run iteratively until the optimal linear coefficient and exponent of the criterion (Eq. 3) used to filter out apparent packets were found (Fig. 6). As objective function we used an equally weighted combination of parameters describing the accuracy of bedload flux and grain-size estimates, i.e.  $r$ ,  $R^2$ ,  $p_{factor\_2}$ ,  $p_{factor\_5}$ , and  $RMSE$  as shown in Table 5,  $r_{D_x}$  as shown in Fig. 11, and the accuracy derived from the confusion matrix (Fawcett, 2006) as shown in Table S2 in Supporting Information. We looked for two types of optimal calibrations. The first type is a general calibration, for which we have presented the results in Sect. 3. This calibration combines all four stations in order to investigate the feasibility of a general signal conversion procedure applicable to multiple sites equipped with SPG systems. The second type is a site-specific calibration aiming to improve the accuracy of bedload transport rate estimates at a single monitoring station, to be used for a more detailed analysis of bedload-related processes at a given site (details of these site-specific calibrations are available in Supporting Information Sect. S4 and S5).

468

469 The biases introduced by apparent packets can be removed by site-specific calibration of the coefficients  $k_{b,i,j}$ , so the  
470 AF and AH methods perform about equally well when calibrated separately to each individual site (see Supporting  
471 Information Sect. S4 and S5). This result supports the use of the AF method, considering the important number of packets  
472 left out by the AF thresholds. However, the abundance of apparent packets varies considerably from site to site, owing to  
473 differences in the channel geometry, the bedload grain-size distribution, and the construction details of the individual SPG  
474 installations. Because the AF method filters out a substantial fraction of these apparent packets, it yields substantially better  
475 general calibrations than the AH method does (see Table 5).

476 We also tested the performance of an adapted version of the AH method introduced by Rickenmann et al. (2018). This  
477 method was originally developed for the Erlenbach site and aimed to correct for the relationship between the signal response  
478 and the transport rate. In the present study, we applied this method to each field site. The only notable improvement  
479 introduced by the adapted AH method is the increased number of detected samples at the Erlenbach station, leading to more  
480 accurate estimates of the various characteristic grain sizes  $D_x$  at this site (Tables S8 and S9 in Supporting Information); the  
481 results for the other sites were not substantially improved.

482 While the lack of accurate flow velocity measurements is certainly one of the critical points of the study, one could  
483 argue that another lack is the low variability between the site-specific calibration relationships of the three natural sites  
484 already before implementing the AF method (Fig. 8a). It would have been interesting to test the method on a larger number  
485 (and variety) of sites. Unfortunately, these four chosen sites are the only ones at which a full geophone signal has been  
486 recorded during calibration measurements.

## 487 4.2 Two-dimensional size class thresholds

488 To understand the performance of the new AF method it is worth taking a closer look at the role of the size class thresholds.  
489 As shown in Fig. 7, replacing the upper amplitude thresholds with amplitude-frequency values results in the following two  
490 important changes. First, a dimension is added, which facilitates focusing on the narrow range of signal responses  
491 characteristic for real packets, and filtering out many of the apparent packets. Second, the areas of the amplitude-frequency  
492 domain covered by two adjacent classes can now overlap. Packets located in overlapping areas are assigned once to each  
493 class and therefore counted twice. This explains why both the number of detected packets  $PACK_j$  (Fig. 7c and 7d) and  
494 subsequently the  $k_{b,j}$  values (Fig. 8) are slightly higher when the AF method (instead of the AH method) is applied to the  
495 larger size classes. Counting such packets twice is not unreasonable, given that the ranges of signal responses recorded  
496 during single-grain-size flume experiments for two contiguous grain-size classes significantly overlap, even after apparent  
497 packets are filtered out (Fig. 5). Overlapping class boundaries therefore results in a less strict classification of the few  
498 packets that are on the edges of the classes. In Fig. 7b, out of 2256 packets recorded by G2 (blue), 144 packets have been  
499 counted twice. But interestingly, not a single of the 153 packets recorded by G1 (red) encompassed by the class boundaries  
500 has been counted twice. A further result supports the use of the two-dimensional size class thresholds. When applying the  
501 AF method, the  $k_{b,j}$  coefficients obtained for the different sites (Fig. 8b) reach a maximum value at the third smallest size  
502 class. A similar yet stronger decrease towards the two smallest classes was described by Wyss et al. (2016b) and was related  
503 to the reduced detectability of the smallest particle sizes.

504 Through the reduced area covered by the new amplitude-frequency thresholds in Fig. 7b, a certain percentage of all the  
505 packets recorded during the field calibration experiments is neglected for general calibration: 55% at the Albula site, 63% at  
506 Navisence, 58% at Avançon de Nant and only 9% at Erlenbach. This suggests that the plates embedded at Erlenbach pick up  
507 less noise from their surroundings. A similar trend was observed by Nicollier et al. (2022) when comparing the maximum  
508 amplitude registered by two adjacent plates for a given impact at the same location. This difference in noise detection levels  
509 is possibly accentuated by the number of impacted plates during bedload transport events. The SPG array embedded in the

510 artificial U-shaped channel of the Erlenbach has the particularity that only 2 out of its 12 plates are usually impacted by  
511 bedload particles during floods (and only sediment crossing these two plates is caught by the automatic basket sampler),  
512 while at the other stations all 10 to 30 embedded plates are submerged by the flow and thus can potentially be impacted.

### 513 4.3 Sampling uncertainties

514 Even though the AF method improved the overall accuracy of flux estimates for most classes (Table 5), some trends  
515 addressed in Sect. 3 suggest that factors other than the noise level also control the accuracy of the estimates. The dataset  
516 presented in this study includes 308 calibration measurements and is in our knowledge the largest dataset gathered for an  
517 impact plate system. Still, it appears that the number of collected samples is not sufficient to accurately assess the  
518 performance of the two methods for the three largest particle-size classes (Fig. 9; Table 5). This is mainly due to the fact that  
519 in typical sediment mixtures, large particles are rarer than fine particles (Rickenmann et al., 2014; Mao et al., 2016). Earlier  
520 investigations have shown that a larger number of detected bedload particles reduces the scatter of total mass estimates by  
521 averaging over stochastic factors such as the impact location on a given impact plate, the particle transport mode (sliding,  
522 rolling, saltating, etc.), and the impact velocity (Rickenmann and McArdell, 2008; Turowski et al., 2013). A further  
523 uncertainty arises because these larger particles are transported at higher bed shear stresses (Einstein, 1950; Wilcock and  
524 Crowe, 2003), which also mobilize more total material and thus pose a serious challenge regarding the sampling efficiency  
525 of the calibration bedload samplers. Bunte and Abt (2005) and Bunte et al. (2019) have demonstrated that reducing the  
526 sampling duration with a bedload trap from 60 to 2 minutes decreases both the sampled unit total bedload flux  $q_{b,tot}$  and the  
527 sampled maximum particle size  $D_{max}$  by about half. In the present study, total bedload fluxes up to  $4 \text{ kg m}^{-1} \text{ s}^{-1}$  were measured  
528 with the net sampler, meaning that the measurement duration had to be minimized to avoid overloading the sampler. At the  
529 Albula stream, for instance, only four samples contained particles of the largest class, and all four were sampled over a  
530 duration ranging from 1 to 2 minutes. As a comparison, the longest sampling duration was reached at the Navisence site and  
531 lasted 25 minutes. All this suggests that an optimal calibration of the SPG system requires balancing the sampling duration  
532 and the number of collected particles. Note that uncertainties in the direct measurements have a direct impact on the  
533 accuracy of fractional sediment flux and grain-size estimates. Flume experiments could potentially be used to assess the  
534 sampling efficiency of the various calibration sampling methods, along with the detection efficiency of the SPG system.

### 535 4.4 Transport rate

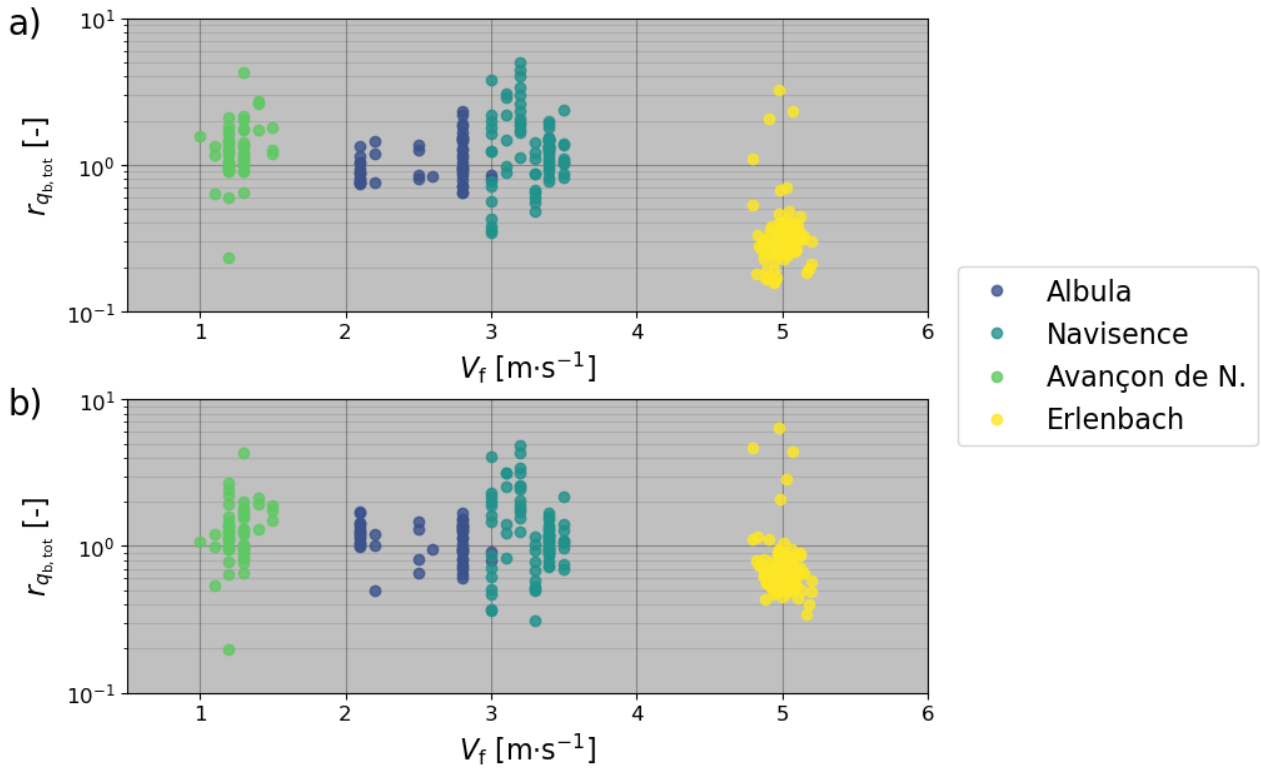
536 Two further trends are evident in the unit fractional flux estimates obtained for the seven smallest classes, for which most  
537 samples were detected ( $N_{\text{samples,est}} / N_{\text{samples,meas}} > 96\%$ ; Table 5). First, the relative scatter (on the log-log plots) of the  
538 fractional flux estimates around the power-law regression lines in Fig. 9 is smaller at higher transport rates. Second, both  
539 total and fractional fluxes are generally overestimated at low transport rates and underestimated at high transport rates (Fig. 9  
540 and 10), which also correspond to the largest calibration samples. These findings agree with results from previous calibration  
541 campaigns with the SPG system (Rickenmann and Fritschi, 2017; Rickenmann et al., 2018) but a comprehensive explanation  
542 for these trends is still missing. The following hypotheses can be put forward to explain the relationship between the mass  
543 flux estimates and the transport rate  $q_b$ : (i) The SPG system may suffer from signal saturation when the transport rate is too  
544 high, as has been documented in the Japanese pipe microphone system (Mizuyama et al., 2011; Choi, 2020). In our SPG data,  
545 we have observed long packets containing multiple large peaks corresponding to several impacts occurring so quickly after  
546 one another that they were not detected as separate packets. One can expect that the probability of occurrence of such  
547 packets increases together with the transport rate, with the transport of large particles (which typically generate packets of  
548 longer durations), and with the occurrence of sliding and rolling particles (Chen et al., 2022). The long packets take the place

549 of multiple shorter packets that would otherwise be individually counted; thus, they lead to underestimated mass fluxes for a  
550 given  $k_{b,j}$  value. The development of a procedure to identify such packets and attribute the therein contained peaks to  
551 individual impacts could represent an interesting goal for future research. (ii) Field observations of bedload sheets being  
552 transported over plates at high transport rates were made at the Vallon de Nant site. In the presence of bedload sheets, one  
553 can expect that the detection rate of transported particles is hampered by multiple particle layers (Rickenmann et al. 1997;  
554 Turowski and Rickenmann, 2009), kinetic sieving (e.g. Frey and Church, 2011) or percolation processes (e.g. Recking et al.,  
555 2009). Given these hypotheses, it would be reasonable to expect a stronger signal response at lower transport rates (Fig. 10)

556 We are not able to give a clear explanation for the overestimates of the characteristic grain size  $D_x$  for finer grain  
557 mixtures and underestimates for coarser grain mixtures (as shown in Fig. 11). A similar trend was also observed by  
558 Rickenmann et al. (2018) for calibration measurements originating from the Erlenbach. We speculate that the decrease of the  
559 detection rate along with increasing transport intensity, as mentioned above, may partly explain this phenomenon.

#### 560 **4.5 Effect of the flow velocity**

561 A recurrent feature in the results presented above is an offset between the estimates obtained for the Erlenbach and those  
562 obtained for the three other stations. A similar offset was observed earlier for linear calibration relations for total bedload  
563 mass between the Erlenbach and other field sites with more natural approach flow conditions (Rickenmann et al., 2014).  
564 Although applying the new amplitude-frequency method has reduced the offset in the present study significantly, it remains  
565 visible for both fractional and total bedload flux estimates (Fig. 9, 10, and 12). At the Erlenbach site, the last 35 meters  
566 upstream of the SPG system consist of an artificial bed with a steep channel slope of 16%, made of large flat embedded  
567 boulders (Roth et al., 2016). This explains the supercritical flow regime with a Froude number around 5.1 (Wyss et al.,  
568 2016c) and a flow velocity  $V_f$  around  $5 \text{ m s}^{-1}$  at the check dam with the geophone sensors (Table S1). Bedload particle  
569 velocity  $V_p$  was introduced by Wyss et al. (2016b, c) as a possible governing parameter affecting the number of particles  
570 detected by the SPG system, fast moving particles being less likely to collide against the Swiss plate geophone than slower  
571 moving ones, which are more frequently in contact with the bed. For the present study, we used  $V_f$  as a proxy for  $V_p$ , even  
572 though bedload particles generally travel more slowly than the fluid that surrounds them (Ancey et al., 2008; Chatanantavet  
573 et al., 2013; Auel et al., 2017). Past flume experiments (Wyss et al., 2016b; Kuhnle et al., 2017) have shown that the  
574 calibration coefficient  $k_{b,j}$  can vary with the flow velocity  $V_f$ , such that a three-fold increase in  $V_f$  can lead to a two-fold  
575 decrease of  $k_{b,j}$ . The better detectability of particles that one could expect from the higher impact energy (Wyss et al. 2016b)  
576 seems to be insufficient to compensate the strong reduction of the number of impacts on a plate with increasing flow  
577 velocities. This possibly arises from the fact that larger flow velocities (without increased turbulence) may also lead to flatter  
578 saltation trajectories, thus decreasing the vertical component of the impact force. Furthermore, bed morphology, bed  
579 roughness and flow velocity play important roles in determining particle transport mode, i.e., sliding, rolling, or saltating  
580 (e.g. Bagnold, 1973; Lajeunesse et al., 2010). Although high flow velocities generally favor the saltating mode (Ancey et al.,  
581 2002; Chen et al., 2022), the shallow flow depths measured at the Erlenbach (in average 0.1 m; Wyss et al. 2016b) may limit  
582 the hop height of larger particles (Amir et al., 2017). Considering all these aspects, we hypothesize that the generally  
583 underestimated transport rates observed for the Erlenbach site mainly arise from the exceptionally high flow velocity and the  
584 related transport mode (Fig. 12). Continuous flow velocity measurements are lacking at the Albula and Navisence sites,  
585 hampering a more detailed analysis of their relationships between flow velocities and detection rates.



586

587 **Figure 12:** Ratio  $r_{q_{b,tot}}$  between the estimated and the measured unit total mass flux as a function of the mean flow velocity  $V_f$ , for  
 588 each collected sample and each station, for the AH method (a) and the AF method (b). The indicated flow velocity corresponds to  
 589 in situ measurements made during (or close in time to) the corresponding calibration measurement. For better readability, a  
 590 random scatter ranging from  $-0.2 \text{ m s}^{-1}$  to  $0.2 \text{ m s}^{-1}$  was added to the stable flow velocity of  $5 \text{ m s}^{-1}$  measured at the Erlenbach site.

591 **4.6 K-fold cross-validation**

592 In a last stage, we tested the robustness of the AH and AF methods by splitting the dataset into calibration and validation  
 593 data. Given that the number of calibration measurements is relatively small and varies between stations, we applied a 4-fold  
 594 cross-validation technique (e.g. Khosravi et al., 2020). The field calibration measurements were distributed over four folds,  
 595 each containing an equal number of calibration measurements from each site (Supporting Information Fig. S4). One after  
 596 another, the folds were used as validation datasets while the remaining three folds were used for calibration. General  
 597 calibration coefficients  $k_{b,j,gen}$  were obtained from the calibration dataset and subsequently applied to the validation data to  
 598 derive flux estimates. Even though each fold contains a total of only 48 samples (12 per site), the results obtained with the 4-  
 599 fold cross-validation procedure support our conclusion that including frequency information in the packet classification  
 600 procedure improves the mean accuracy of the estimates over all sites, in particular for the smaller five to six size classes  $j$   
 601 (Supporting Information Table S10). Nicollier et al. (2022) found that most apparent packets are detected as belonging to  
 602 smaller size classes than the particles that caused them, due to the attenuation of the vibrations as they propagate (see Fig. 7).  
 603 It is therefore reasonable that the AF method mainly improves the flux estimates for these smaller classes.

604 **5 Conclusion**

605 The Swiss plate geophone (SPG) is a bedload surrogate monitoring system that has been installed in several gravel-bed  
 606 streams and was calibrated using direct sampling techniques. While most site-specific calibration relationships for total mass  
 607 flux are robust across multiple orders of magnitude, the mean calibration coefficients can still vary by about a factor of six  
 608 between different sites. In this study, we derived a general procedure to convert SPG signals into fractional bedload fluxes

609 using an extensive dataset comprising controlled flume experiments as well as 308 field calibration measurements from four  
610 field sites. The proposed hybrid approach is based on previous findings (Antoniazza et al., 2020; Nicollier et al., 2022) that  
611 the SPG system is biased by elastic waves that propagate through the apparatus and generate noise in the form of spurious  
612 “apparent” packets. We introduced the amplitude-frequency (AF) method as an alternative to the amplitude-histogram (AH)  
613 method developed by Wyss et al. (2016a). Packets recorded during single-grain-size flume experiments were first filtered to  
614 exclude apparent packets, and then used to derive grain-size class thresholds for packet classification. We found that filtering  
615 out apparent packets results in more consistent relationships between particle diameter and amplitude-frequency  
616 characteristics of the SPG signal. Furthermore, we showed that including frequency information in size class thresholds  
617 helps in excluding apparent packets and thus improves the signal-to-noise ratio. In a second stage, we applied these flume-  
618 based thresholds to field calibration measurements and derived general calibration coefficients applicable at all four sites for  
619 ten different grain-size fractions. The AH method, by contrast, requires site-specific calibration because it cannot account for  
620 the site-to-site differences in the abundance of apparent packets. Averaged over the ten grain-size fractions, the bedload  
621 masses of 69% and 96% of the samples were estimated within an offset of a factor of two and five, respectively, relative to  
622 the measured sampled masses. The remaining discrepancies between the site-specific results are mainly attributed to large  
623 differences in flow (and probably particle) velocity. Finally, the sampled mass, the transport rate and the sampling efficiency  
624 were identified as further factors possibly influencing the accuracy of mass flux and grain-size estimates.

625 The presented results are highly encouraging regarding future applications of surrogate monitoring methods to  
626 investigate bedload transport processes. The findings also underline the valuable contribution of flume experiments to our  
627 understanding of the relationship between bedload transport and the recorded SPG signal. But above all, this study highlights  
628 the requirements for obtaining calibrations that are transferable across sites: accurate and numerous direct sampling  
629 measurements with long sampling durations and large sampled masses, sensors insulated from surrounding noise sources,  
630 and highly resolved temporal information about the stream flow, to identify and account for variations in the transport  
631 conditions.

## 632 Notation

633	$a_c$	Linear coefficient of the criterion
634	$A_{\text{FFT}}$	Fourier amplitude
635	$A_{m,j}$	Mean amplitude registered for particle-size class $j$
636	$b_c$	Linear coefficient of the criterion
637	$\Delta t_i$	Sampling duration
638	$D_{m,j}$	Mean particle diameter for particle-size class $j$
639	$D_{\text{sieve},j}$	Lower sieve size retaining particle class $j$
640	$D_x$	Characteristic grain size
641	$f_{\text{centroid}}$	Centroid frequency
642	$i$	Sample index
643	$j$	Particle-size class index
644	$k_{b,i,j}$	Sample- and class-specific calibration coefficient
645	$k_{b,j,\text{med,station}}$	Median calibration coefficient for particle-size class $j$ and a given station
646	$k_{b,j,\text{gen}}$	General calibration coefficient for particle-size class $j$
647	$M_{\text{est},i,j}$	Estimated fractional mass per sample and per class
648	$M_{\text{meas},i,j}$	Sampled fractional mass per sample and per class
649	$\text{MaxAmp}_{\text{env}}$	Maximum registered amplitude within a packet

650	$N_{\text{samples,est}}$	Number of detected samples
651	$N_{\text{stations}}$	Number of stations
652	$PACK_{i,j}$	Number of recorded packets per sample and per class
653	$p_{\text{factor}_x}$	Percentage of all detected samples for which the estimated and the measured values differ from each other by less than a factor of $x$
654		
655	$q_{b,est,i,j}$	Estimated unit fractional transport rate per sample and per class
656	$q_{b,meas,i,j}$	Measured unit fractional transport rate per sample and per class
657	$q_{b,tot,est,i}$	Estimated unit total bedload flux per sample
658	$q_{b,tot,meas,i}$	Measured unit total bedload flux per sample
659	$R^2$	Coefficient of determination
660	$r$	Correlation coefficient
661	$r_x$	Ratio between estimated and measured values $x$
662	$th_{ah,j}$	Amplitude-histogram thresholds
663	$th_{af,low,j}$	Lower amplitude-frequency thresholds
664	$th_{af,up,j}$	Upper amplitude-frequency thresholds
665	$V_f$	Mean flow velocity
666	$w_p$	Standard width of an impact plate

## 667 **Data availability**

668 The dataset presented in this paper is available online on the EnviDat repository

669 <https://www.envidat.ch/#/metadata/sediment-transport-observations-in-swiss-mountain-streams>.

## 670 **Author contribution**

671 Tobias Nicollier designed and carried out the field and flume experiments, developed the presented workflow and prepared  
672 the manuscript with contributions from all co-authors. Gilles Antoniazza designed and carried out the field experiments at  
673 the Vallon de Nant site. Lorenz Ammann helped developing the methodology and contributed to the formal analysis. Dieter  
674 Rickenmann contributed to the conceptualization and the supervision of the presented work, contributed to the design of the  
675 methodology, and provided support during the field and flume experiments. James W. Kirchner contributed to the  
676 development of the methodology and significantly contributed to the preparation of the initial draft.

## 677 **Acknowledgements**

678 This study was supported by Swiss National Science Foundation (SNSF) grant 200021L\_172606, and by Deutsche  
679 Forschungsgemeinschaft (DFG) grant RU 1546/7-1. The authors are grateful to Arnd Hartlieb, to the students of the TU  
680 Munich, and to the technical staff of the Oskar von Miller Institute for helping to set up and perform the flume experiments.  
681 They also warmly thank Norina Andres, Mehdi Mattou, Nicolas Steeb, Florian Schläfli, Konrad Eppel and Jonas von  
682 Wartburg for their efforts and motivation during the field calibration campaigns. Special thanks go to Stefan Boss for his  
683 support with the measurement systems at all sites, and to Andreas Schmucki, who never gave up repairing the net sampler.  
684 Alexandre Badoux is further thanked for his valuable suggestions regarding an earlier version of the manuscript.



685 **Competing interests**

686 The authors declare that they have no conflict of interest.

687 **References**

- 688 Amir, M., Nikora, V., and Witz, M.: A novel experimental technique and its application to study the effects of particle  
689 density and flow submergence on bed particle saltation, *J. Hydraul. Res.*, 55, 101–113,  
690 <https://doi.org/10.1080/00221686.2016.1233583>, 2017.
- 691 Ancey, C., Bigillon, F., Frey, P., Lanier, J., and Ducret, R.: Saltating motion of a bead in a rapid water stream, *Phys. Rev. E*,  
692 66, p. 036306, <https://doi.org/10.1103/PhysRevE.66.036306>, 2002.
- 693 Ancey, C., Davison, A. C., Böhm, T., Jodeau, M., and Frey, P.: Entrainment and motion of coarse particles in a shallow  
694 water stream down a steep slope, *J. Fluid Mech.*, 595, 83–114, <https://doi.org/10.1017/S0022112007008774>, 2008.
- 695 Ancey, C.: Bedload transport: a walk between randomness and determinism. Part 2. Challenges and prospects, *J. Hydraul.*  
696 *Res.*, 58, 18–33, <https://doi.org/10.1080/00221686.2019.1702595>, 2020.
- 697 Antoniazza, G., Nicollier, T., Wyss, C. R., Boss, S., and Rickenmann, D.: Bedload transport monitoring in alpine rivers:  
698 Variability in Swiss plate geophone response, *Sensors*, 20, <https://doi.org/10.3390/s20154089>, 2020.
- 699 Antoniazza, G., Nicollier, T., Boss, S., Mettra, F., Badoux, A., Schaepli, B., Rickenmann, D., and Lane, S.: Hydrological  
700 drivers of bedload transport in an Alpine watershed, *Water Resour. Res.*, 58, e2021WR030663,  
701 <https://doi.org/10.1029/2021WR030663>, 2022.
- 702 Auel, C., Albayrak, I., Sumi, T., and Boes, R. M.: Sediment transport in high-speed flows over a fixed bed: 1. Particle  
703 dynamics, *Earth Surf. Processes Landforms*, 42, 1365–1383, <https://doi.org/10.1002/esp.4128>, 2017.
- 704 Badoux, A., Andres, N. and Turowski, J.M.: Damage costs due to bedload transport processes in Switzerland, *Nat. Hazards*  
705 *and Earth Syst. Sci.*, 14(2), 279–294, <https://doi.org/10.5194/nhess-14-279-2014>, 2014.
- 706 Bagnold, R. A.: The nature of saltation and of bed-load transport in water. *Proc. Royal Soc. A, London, England*, 332, 473–  
707 504, <https://doi.org/10.1098/rspa.1973.0038>, 1973.
- 708 Bakker, M., Gimbert, F., Geay, T., Misset, C., Zanker, S., and Recking, A.: Field application and validation of a seismic  
709 bedload transport model, *J. Geophys. Res.*, 125, e2019JF005416, <https://doi.org/10.1029/2019JF005416>, 2020.
- 710 Barrière, J., Krein, A., Oth, A., and Schenkluhn, R.: An advanced signal processing technique for deriving grain size  
711 information of bedload transport from impact plate vibration measurements, *Earth Surf. Processes Landforms*,  
712 <https://doi.org/10.1002/esp.3693>, 2015.
- 713 Bathurst, J. C.: Effect of coarse surface layer on bed-load transport, *J. Hydraul. Eng.*, 133(11), 1192–1205,  
714 [https://doi.org/10.1061/\(ASCE\)0733-9429\(2007\)133:11\(1192\)](https://doi.org/10.1061/(ASCE)0733-9429(2007)133:11(1192)), 2007.
- 715 Belleudy, P., Valette, A., and Graff, B.: Passive hydrophone monitoring of bedload in river beds: First trials of signal  
716 spectral analyses, *U.S. Geol. Surv. Sci. Invest. Rep.*, 2010-5091, 67–84, 2010.
- 717 Blöschl, G., Kiss, A., Viglione, A., Barriendos, M., Böhm, O., Brázdil, R., et al.: Current European flood-rich period  
718 exceptional compared with past 500 years, *Nature*, 583(7817), 560–566, <https://doi.org/10.1038/s41586-020-2478-3>, 2020.

719 Bogen, J., and Møen, K.: Bed load measurements with a new passive acoustic sensor, in Erosion and Sediment Transport  
720 Measurement in Rivers: Trends and Explanation, *IAHS Publications*, 283, 181-182, 2003.

721 Brouwer, R., and Sheremet, O. I.: The economic value of river restoration, *Water Resour. Eco.*, 17, 1-8,  
722 <https://doi.org/10.1016/j.wre.2017.02.005>, 2017.

723 Bunte, K., Abt, S. R., Potyondy, J. P., and Ryan, S. E.: Measurement of coarse gravel and cobble transport using a portable  
724 bedload trap, *J. Hydraul. Eng.*, 130(9), 879-893, [https://doi.org/10.1061/\(ASCE\)0733-9429\(2004\)130:9\(879\)](https://doi.org/10.1061/(ASCE)0733-9429(2004)130:9(879)), 2004.

725 Bunte, K., and Abt, S. R.: Effect of sampling time on measured gravel bed load transport rates in a coarse-bedded stream,  
726 *Water Resour. Res.*, 41, W11405, <https://doi.org/10.1029/2004WR003880>, 2005.

727 Bunte, K., Abt, S. R., Cenderelli, D. A., Ettema, R., and Swingle, K. W.: Bedload traps and Helley-Smith Sampler Collect  
728 Different Rates and Particle Sizes of Gravel Bedload, *Proceedings of the SEDHYD 2019 Conference, Federal Interagency  
729 Sedimentation and Hydrologic, Modeling Conference*, Reno, NV, 2019.

730 Chatanantavet, P., Whipple, K. X., Adams, M. A., and Lamb, M. P.: Experimental study on coarse grain saltation dynamics  
731 in bedrock channels, *J. Geophys. Res.*, 118, 1161–1176, <https://doi.org/10.1002/jgrf.20053>, 2013.

732 Chen, Z., He, S., Nicollier, T., Ammann, L., Badoux, A., and Rickenmann, D.: Signal response of the Swiss plate geophone  
733 monitoring system impacted by bedload particles with different transport modes, *Earth Surf. Dyn.*, 10(2): 279-300,  
734 <https://doi.org/10.5194/esurf-10-279-2022>, 2022.

735 Choi, J. H., Jun, K. W., and Jang, C. D.: Bed-Load Collision Sound Filtering through Separation of Pipe Hydrophone  
736 Frequency Bands, *Water*, 12, 1875, <https://doi.org/10.3390/w12071875>, 2020.

737 Church, M., Hassan, M. A., and Wolcott, J. F.: Stabilizing self-organized structures in gravel-bed stream channels: Field and  
738 experimental observations, *Water Resour. Res.*, 34(11), 3169–3179, <https://doi.org/10.1029/98WR00484>, 1998.

739 Dell'Agnese, A., Mao, L., and Comiti, F.: Calibration of an acoustic pipe sensor through bedload traps in a glacierized basin,  
740 *CATENA*, 121, 222-231, <https://doi.org/10.1016/j.catena.2014.05.021>, 2014.

741 Detert, M., and Weitbrecht, V.: User guide to gravelometric image analysis by BASEGRAIN, *Adv. Sci. Res.*, S. Fukuoka, H.  
742 Nakagawa, T. Sumi, H. Zhang (Eds.), Taylor and Francis Group, London, ISBN 978-1-138-00062-9, 1789-1795, 2013.

743 Dhont, B., and Ancy, C.: Are bedload transport pulses in gravel bed rivers created by bar migration or sediment waves?  
744 *Geophys. Res. Lett.*, 45, 5501– 5508, <https://doi.org/10.1029/2018GL077792>, 2018.

745 Einstein, H. A.: The Bedload Transport as Probability Problem, *Mitteilung der Versuchsanstalt für Wasserbau an der  
746 Eidgenössischen Technischen Hochschule*, Zürich, Switzerland, 1937.

747 Einstein, H. A.: The Bedload Transport as Probability Problem, *Technical bulletin*, 1026, United States Department of  
748 Agriculture, Soil Conservation Service, Washington, DC, 1950.

749 Fawcett, T.: An introduction to ROC analysis, *Pattern Recognit. Lett.*, 27 (8), 861-874,  
750 <https://doi.org/10.1016/j.patrec.2005.10.010>, 2006.

751 Frey, P., and Church, M.: Bedload: a granular phenomenon, *Earth Surf. Processes Landforms*, 36, 58-69,  
752 <https://doi.org/10.1002/esp.2103>, 2011.

753 Geay, T., Zanker, S., Misset, C., and Recking, A.: Passive Acoustic Measurement of Bedload Transport: Toward a Global  
754 Calibration Curve?, *J. Geophys. Res.*, *125*, <https://doi.org/10.1029/2019JF005242>, 2020.

755 Gray, J. R., Laronne, J. B., Marr, J. D. G. (eds): Bedload-surrogate Monitoring Technologies, *U.S. Geol. Surv. Sci. Invest.*  
756 *Rep.*, 2010–5091, US Geological Survey: Reston, VA, <http://pubs.usgs.gov/sir/2010/5091/>, 2010.

757 Habersack, H., Kreisler, A., Rindler, R., Aigner, J., Seitz, H., Liedermann, M., and Laronne, J. B.: Integrated automatic and  
758 continuous bedload monitoring in gravel bed rivers, *Geomorphology*, *291*, 80–93,  
759 <https://doi.org/10.1016/j.geomorph.2016.10.020>, 2017.

760 Halfi, E., Paz, D., Stark, K., Yogev, U., Reid, I., Dorman, M., and Laronne, J. B.: Novel mass-aggregation-based calibration  
761 of an acoustic method of monitoring bedload flux by infrequent desert flash floods, *Earth Surf. Processes Landforms*, *45*,  
762 3510-3524, <https://doi.org/10.1002/esp.4988>, 2020.

763 Hilldale, R. C., Carpenter, W. O., Goodwiller, B., Chambers, J. P. and Randle, T. J.: Installation of impact plates to  
764 continuously measure bed load: Elwha River, Washington, USA, *J. Hydraul. Eng.*, *141*(3),  
765 [https://doi.org/10.1061/\(ASCE\)HY.1943-7900.0000975](https://doi.org/10.1061/(ASCE)HY.1943-7900.0000975), 2015.

766 Johnson, K.: Contact Mechanics, Cambridge: Cambridge University Press, <https://doi.org/10.1017/CBO9781139171731>,  
767 1985.

768 Jones, E., Oliphant, T., and Peterson, P.: SciPy: Open source scientific tools for Python [Cited 2021 December 29],  
769 Available from: <http://www.scipy.org>, 2002.

770 Khosravi, K., Cooper, J. R., Daggupati, P., Thai Pham, B., and Bui, D. T.: Bedload transport rate prediction: Application of  
771 novel hybrid data mining techniques, *J. Hydrol.*, *585*, 124774, <https://doi.org/10.1016/j.jhydrol.2020.124774>, 2020.

772 Koshiha, T., and Sumi, T.: Application of the wavelet transform to sediment grain sizes analysis with an impact plate for  
773 bedload monitoring in sediment bypass tunnels, *E3S Web of Conferences*, *40*, 04022,  
774 <https://doi.org/10.1051/e3sconf/20184004022>, 2018.

775 Krein, A., Klinck, H., Eiden, M., Symader, W., Bierl, R., Hoffmann, L., and Pfister, L.: Investigating the transport dynamics  
776 and the properties of bedload material with a hydro-acoustic measuring system, *Earth Surf. Processes Landforms*, *33*, 152–  
777 163, <https://doi.org/10.1002/esp.1576>, 2008.

778 Kreisler, A., Moser, M., Aigner, J., Rindler, R., Tritthard, M., and Habersack, H.: Analysis and classification of bedload  
779 transport events with variable process characteristics, *Geomorphology*, *291*, 57–68,  
780 <https://doi.org/10.1016/j.geomorph.2016.06.033>, 2017.

781 Kuhnle, R., Wren, D., Hilldale, R. C., Goodwiller, B., and Carpenter, W.: Laboratory Calibration of Impact Plates for  
782 Measuring Gravel Bed Load Size and Mass, *J. Hydraul. Eng.*, *143*, [https://doi.org/10.1061/\(ASCE\)HY.1943-7900.0001391](https://doi.org/10.1061/(ASCE)HY.1943-7900.0001391),  
783 2017.

784 Lajeunesse, E., Malverti, L., and Charru, F.: Bed load transport in turbulent flow at the grain scale: Experiments and  
785 modeling, *J. Geophys. Res.*, *115*, F04001, <https://doi.org/10.1029/2009JF001628>, 2010.

786 Le Guern, J., Rodrigues, S., Geay, T., Zanker, S., Hauet, A., Tassi, P., et al.: Relevance of acoustic methods to quantify  
787 bedload transport and bedform dynamics in a large sandy-gravel-bed river, *Earth Surf. Dyn.*, *9*, 423–444,  
788 <https://doi.org/10.5194/esurf-9-423-2021>, 2021.

789 Logar, I., Brouwer, R., and Paillex, A.: Do the societal benefits of river restoration outweigh their costs? A cost-benefit  
790 analysis, *J. Environ. Manage.*, 232, 1075–1085, <https://doi.org/10.1016/j.jenvman.2018.11.098>, 2019.

791 Manga, M., and Kirchner, J. W.: Stress partitioning in streams by large woody debris, *Water Resour. Res.*, 36(8), 2373-2379,  
792 <https://doi.org/10.1029/2000WR900153>, 2000.

793 Mao, L., Carrillo, R., Escarriaza, C., and Iroume, A.: Flume and field-based calibration of surrogate sensors for monitoring  
794 bedload transport, *Geomorphology*, 253, 10-21, <https://doi.org/10.1016/j.geomorph.2015.10.002>, 2016.

795 Mizuyama, T., Hirasawa, R., Kosugi, K., Tsutsumi, D., and Nonaka, M.: Sediment monitoring with a hydrophone in  
796 mountain torrents, *Int. J. Erosion Control Eng.*, 4(2), 43–47, <https://doi.org/10.13101/ijece.4.43>, 2011.

797 Mühlhofer, L.: Untersuchungen über die Schwebstoff und Geschiebeführung des Inn nächst Kirchbichl (Tirol), *Die*  
798 *Wasserwirtschaft*, 1(6), 23 pp, 1933.

799 Nicollier, T., Rickenmann, D., and Hartlieb, A.: Field calibration of the Swiss plate geophone system at the Albula stream  
800 and comparison with controlled flume experiments, 8 pp., Paper presented at the SEDHYD 2019 Conference, Reno, NV,  
801 2019.

802 Nicollier, T., Rickenmann, D., Boss, S., Travaglini, E., and Hartlieb, A.: Calibration of the Swiss plate geophone system at  
803 the Zinal field site with direct bedload samples and results from controlled flume experiments, in River Flow 2020,  
804 *Proceedings of the 10th Conference on Fluvial Hydraulics*, 901–909, <https://doi.org/10.1201/b22619>, 2020.

805 Nicollier, T., Rickenmann, D., and Hartlieb, A.: Field and flume measurements with the impact plate: Effect of bedload  
806 grain-size distribution on signal response, *Earth Surf. Processes Landforms*, 17 pp., <https://doi.org/10.1002/esp.5117>, 2021.

807 Nicollier, T., Antoniazza, G., Rickenmann, D., Hartlieb, A., and Kirchner, J.W.: Improving the calibration of impact plate  
808 bedload monitoring systems by filtering out acoustic signals from extraneous particle impacts. *Earth Space Sci.*, 9,  
809 e2021EA001962, <https://doi.org/10.1029/2021EA001962>, 2022.

810 Nitsche, M., Rickenmann, D., Turowski, J. M., Badoux, A., and Kirchner, J. W.: Evaluation of bedload transport predictions  
811 using flow resistance equations to account for macro-roughness in steep mountain streams, *Water Resour. Res.*, 47, W08513,  
812 <https://doi.org/10.1029/2011WR010645>, 2011.

813 Pauli, M., Hunzinger, L., and Hitz, O.: More bed load in rivers. Achieving a sediment balance close to the natural state, *J.*  
814 *Appl. Water Eng. Res.*, 6(4), 274–282, <https://doi.org/10.1080/23249676.2018.1497554>, 2018.

815 Piantini, M., Gimbert, F., Bellot, F., and Recking, A.: Triggering and propagation of exogenous sediment pulses in mountain  
816 channels: insights from flume experiments with seismic monitoring, *Earth Surf. Dyn.*, 9, 1423–1439,  
817 <https://doi.org/10.5194/esurf-9-1423-2021>, 2021.

818 Prancevic, J. P., and Lamb, M. P.: Unraveling bed slope from relative roughness in initial sediment motion, *J. Geophys. Res.*,  
819 120, 474–489, <https://doi.org/10.1002/2014JF003323>, 2015.

820 Rachelly, C., Friedl, F., Boes, R. M., and Weitbrecht, V.: Morphological response of channelized, sinuous gravel-bed rivers  
821 to sediment replenishment, *Water Resour. Res.*, 57, e2020WR029178, <https://doi.org/10.1029/2020WR029178>, 2021.

822 Recking, A., Frey, P., Paquier, A., and Belleudy, P.: An experimental investigation of mechanisms involved in bed load  
823 sheet production and migration, *J. Geophys. Res.*, 114, F03010, <https://doi.org/10.1029/2008JF000990>, 2009.

824 Reid, I., Frostick, L. E., and Layman, J.T.: The incidence and nature of bedload transport during flood flows in coarse-  
825 grained alluvial channels, *Earth Surf. Processes Landforms*, 10, 33-44, <https://doi.org/10.1002/esp.3290100107>, 1985.

826 Rickenmann, D.: Bed-load transport measurements with geophones and other passive acoustic methods, *J. Hydraul. Eng.*,  
827 143(6), 03117004-1-14, [https://doi.org/10.1061/\(ASCE\)HY.1943-7900.0001300](https://doi.org/10.1061/(ASCE)HY.1943-7900.0001300), 2017.

828 Rickenmann, D.: Effect of sediment supply on cyclic fluctuations of the disequilibrium ratio and threshold transport  
829 discharge, inferred from bedload transport measurements over 27 years at the Swiss Erlenbach stream, *Water Resour. Res.*,  
830 56, e2020WR027741, <https://doi.org/10.1029/2020WR027741>, 2020.

831 Rickenmann, D., and McArdell, B. W.: Calibration measurements with piezoelectric bedload impact sensors in the Pitzbach  
832 mountain stream, *Geodin. Acta*, 21, 35–52, <https://doi.org/10.3166/ga.21.35-52>, 2008.

833 Rickenmann, D., and Recking, A.: Evaluation of flow resistance in gravel-bed rivers through a large field data set, *Water*  
834 *Resour. Res.*, 47, W07538, <https://doi.org/10.1029/2010WR009793>, 2011.

835 Rickenmann, D., and Fritschi, B.: Bedload transport measurements with impact plate geophones in two Austrian mountain  
836 streams (Fischbach and Ruetz): system calibration, grain size estimation, and environmental signal pick-up, *Earth Surf.*  
837 *Dyn.*, 5(4): 669-687, <https://doi.org/10.5194/esurf-5-669-2017>, 2017.

838 Rickenmann, D., Hofer, B., and Fritschi, B.: Geschiebemessung mittels Hydrophon, *Österreichische Wasser- und*  
839 *Abfallwirtschaft*, 49(11/12). 219-228, 1997.

840 Rickenmann, D., Turowski, J. M., Fritschi, B., Klaiber, A., and Ludwig, A.: Bedload transport measurements at the  
841 Erlenbach stream with geophones and automated basket samplers, *Earth Surf. Processes Landforms*, 37(9), 1000–1011,  
842 <https://doi.org/10.1002/esp.3225>, 2012.

843 Rickenmann, D., Turowski, J. M., Fritschi, B., Wyss, C., Laronne J.B., Barzilai, R., et al.: Bedload transport measurements  
844 with impact plate geophones: comparison of sensor calibration in different gravel-bed streams, *Earth Surf. Processes*  
845 *Landforms*, 39, 928– 942, <https://doi.org/10.1002/esp.3499>, 2014.

846 Rickenmann, D., Steeb, N., and Badoux, A.: Improving bedload transport determination by grain-size fraction using the  
847 Swiss plate geophone recordings at the Erlenbach stream, in River Flow 2018, *Proceedings of the 9th Int. Conference on*  
848 *Fluvial Hydraulics*, 8 pp., <https://doi.org/10.1051/e3sconf/20184002009>, 2018.

849 Roth, D. L., Brodsky, E. E., Finnegan, N. J., Rickenmann, D., Turowski, J.M., and Badoux, A.: Bed load sediment transport  
850 inferred from seismic signals near a river, *J. Geophys. Res.*, 121, 725-747, <https://doi.org/10.1002/2015JF003782>, 2016.

851 Schneider, J. M., Rickenmann, D., Turowski, J. M., Schmid, B., and Kirchner, J. W.: Bed load transport in a very steep  
852 mountain stream (Riedbach, Switzerland): Measurement and prediction, *Water Resour. Res.*, 52, 9522–9541,  
853 <https://doi.org/10.1002/2016WR019308>, 2016.

854 Thorne, P. D.: Laboratory and marine measurements on the acoustic detection of sediment transport, *J. Acoust. Soc. Am.*, 80,  
855 899–910, <https://doi.org/10.1121/1.393913>, 1986.

856 Tsakiris, A. G., Papanicolaou, A. N., and Lauth, T.: Signature of bedload particle transport mode in the acoustic signal of a  
857 geophone, *J. Hydraul. Res.*, 52, 185–204, <https://doi.org/10.1080/00221686.2013.876454>, 2014.

858 Turowski, J.M., and Rickenmann, D.: Tools and cover effect in the Pitzbach, Austria, *Earth Surf. Processes Landforms*, 34,  
859 26–37, <https://doi.org/10.1002/esp.1686>, 2009.

860 Turowski, J. M., Bockli, M., Rickenmann, D., and Beer, A. R.: Field measurements of the energy delivered to the channel  
861 bed by moving bed load and links to bedrock erosion, *J. Geophys. Res.*, 118, 2438–2450,  
862 <https://doi.org/10.1002/2013JF002765>, 2013.

863 Uher, M., and Benes, P.: Measurement of particle size distribution by acoustic emission method, paper presented at XX  
864 IMEKO World Congress, Busan, South Korea, 2012.

865 Wilcock, P.R., and Crowe, J.C.: A surface-based transport model for sand and gravel, *J. Hydraul. Eng.*, 129(2), 120-128,  
866 [https://doi.org/10.1061/\(ASCE\)0733-9429\(2003\)129:2\(120\)](https://doi.org/10.1061/(ASCE)0733-9429(2003)129:2(120)), 2003.

867 Wyss, C. R., Rickenmann, D., Fritschi, B., Turowski, J., Weitbrecht, V., and Boes, R.: Measuring bed load transport rates by  
868 grain-size fraction using the Swiss plate geophone signal at the Erlenbach, *J. Hydraul. Eng.*, 142(5),  
869 [https://doi.org/10.1061/\(ASCE\)HY.1943-7900.0001090,04016003](https://doi.org/10.1061/(ASCE)HY.1943-7900.0001090,04016003), 2016a.

870 Wyss, C. R., Rickenmann, D., Fritschi, B., Turowski, J., Weitbrecht, V., and Boes, R.: Laboratory flume experiments with  
871 the Swiss plate geophone bed load monitoring system: 1. Impulse counts and particle size identification, *Water Resour. Res.*,  
872 52, 7744–7759, <https://doi.org/10.1002/2015WR018555>, 2016b.

873 Wyss, C. R., Rickenmann, D., Fritschi, B., Turowski, J., Weitbrecht, V., Travaglini E, et al.: Laboratory flume experiments  
874 with the Swiss plate geophone bed load monitoring system: 2. Application to field sites with direct bed load samples, *Water*  
875 *Resour. Res.*, 52, 7760–7778, <https://doi.org/10.1002/2016WR019283>, 2016c.

876 Yager, E. M., Kirchner, J. W., and Dietrich, W. E.: Calculating bed load transport in steep boulder bed channels, *Water*  
877 *Resour. Res.*, 43, W07418, <https://doi.org/10.1029/2006WR005432>, 2007.

878 Yager, E. M., Dietrich, W. E., Kirchner, J. W., and McArdell, B. W.: Prediction of sediment transport in step-pool channels,  
879 *Water Resour. Res.*, 48, W01541, <https://doi.org/10.1029/2011WR010829>, 2012.

880

881

882

883

884